CrossMark

Effect of Alkali-Silica Reactivity Damage to Tip-Over Impact Performance of Dry Cask Storage Structures

Masoud Dehghani Champiri[1],* , Mir Mohammad Reza Mousavi[1], Kaspar Jodok Willam[1], and Bora Gencturk[2]

Abstract: This paper investigates the effect of concrete degradation due to alkali-silica reactivity (ASR) and its effect on the performance of vertical concrete casks in the case of a hypothetical tip-over event. ASR is one of the major problems in certain concrete structures exposed to high relative humidity and temperature. Using the first order kinetic model, the mechanical and environmental effects of degradation are modeled for a dry-cask storage structure under the conditions that ASR is completely extended. Following the degradation, a tip-over impact simulation was performed and compared with that of an intact cask in terms of failure modes, damage patterns, stresses, and accelerations. It was seen that concrete crushing and shear banding are major failure modes in the cask with intact concrete, but in the case of the ASR affected cask, the concrete is fully damaged and a longitudinal crack which separates the cask into two parts propagates through the outerpack.

Keywords: impact analysis, alkali-silica reaction, dry cask storage structures, concrete degradation, failure analysis.

1. Introduction

Degradation of concrete limits the service life of structures. Creep and shrinkage due to moisture transfer in the early age of concrete and expansion due to thermal effects and alkali-silica reaction (ASR) may degrade the concrete properties. Dry cask storage structures in the form of thick-walled cylinders are widely used for storage of spent nuclear fuel. The US Nuclear Regulatory Commission provides regulations to investigate their performance under hypothetical events (Dilger et al. 2012; Halstead and Dilger 2006). A dry cask structure needs to be designed to safeguard the internals under a tip-over impact scenario. Expansion of ASR gel between aggregate and cement paste reduces the stiffness and strength of concrete and may cause cracking (Champiri et al. 2012). Substantial experimental work was performed by Larive (1998) to evaluate the ASR expansion in concrete. Similarly, work has been done to evaluate the tip-over impact performance of dry cask storage structures.

Many researchers worked on hypothetical events including tip-over, drop test and free drop test of concrete cylinders with different geometries. Gupta (1997) proposed a mathematical approach for tip-over simulation. He assumed a rigid pad and a single degree-of-freedom mass-spring system. Other researchers used finite element (FE) method which is now extensively applied for crash simulations. Since implicit time integration is not capable of simulating this contact–impact problem due to the convergence issues with regard to the large deformations and rotations and high nonlinearity, explicit time integration is generally used. Teng et al. (2003) used a dynamic explicit FEA code, named DYNTRAN (2008) for impact analysis of a cask. Elfahal (2003) performed an experimental and numerical study to investigate the size effect in normal and high strength concrete cylinders subjected to static and dynamic axial compressive loads. Lee et al. (2005) simulated the drop impact of a cask using LS-DYNA (Hallquist 2006) and ABAQUS (Hibbitt, Karlsson and Sorensen, Incorporated 2002). Kim et al. (2007) studied shock-absorption characteristics of concrete pads for casks using ABAQUS explicit (Hibbitt, Karlsson and Sorensen, Incorporated 2002). Champiri et al. (2015a, b, 2016) investigated the behavior of a degraded concrete dry cask storage structure under drop test and tip-over event using LS-DYNA (Hallquist 2006). However, the performance of a dry cask structure affected by ASR expansion under tip-over event has not been studied in detail to our knowledge.

Two general methods are presented in the literature to model the macroscopic behavior of ASR. One is a parametric model and the other is a chemo-mechanical coupling model. Léger et al. (1996) showed that the concrete expansion is a function of the compressive stress state,

---

[1]Cullen College of Engineering Building 1, Civil and Environmental Engineering, 4726 Calhoun Road, Room N110, Houston, TX 77204-4003, USA.
*Corresponding Author; E-mail: masoud4060@gmail.com
[2]Sonny Astani Department of Civil and Environmental Engineering, KAP 234B, Kaprielian Hall, 3620 South Vermont Ave., Los Angeles, CA 90089, USA.

temperature, moisture, and reactivity of the concrete constituents. Considering a particular zone, m, in their model, the ASR induced strain is given by

$$\varepsilon_{asr}^m = \beta^m(t)[F_C(\sigma_c, t) \cdot F_T(t) \cdot F_M(t) \cdot F_R(t)]^m = \beta^m(t) \cdot CTMR^m \tag{1}$$

where F_C, F_T, F_M, and F_R are normalized expansion factors (between zero and one) corresponding to compressive stress (σ_c) state, temperature, moisture, and reactivity, respectively, t is the time of reaction, $CTMR^m$ is the normalized ASR induced strain, and β^m is a calibration factor to adjust the numerical results to the experimental results. Huang and Pietruszczak (1996) investigated the mechanical effects of ASR in concrete structures with the assumption that the progress of ASR is coupled with the degradation of mechanical properties. The expansion rate is controlled by the alkali content in the cement, the magnitude of confining stress and temperature. In their model, the degradation functions for Young's modulus, E, and compressive strength, f_c, are defined as

$$E = E_0(1 - (1 - \beta_1)\zeta) \tag{2}$$

$$f_c = f_{c0}(1 - (1 - \beta_2)\zeta) \tag{3}$$

where E_0, f_{c0} are the initial values of Young's modulus and compressive strength, respectively, β_1, β_2 are the material constants and ζ is the ASR index which is between 0 for undeveloped ASR to 1 for fully-developed ASR. Ulm et al. (2000) developed a chemo-elastic model for ASR kinetics and swelling effects. Farage et al. (2004) developed a smeared crack FE approach to analyze the ASR effects in concrete structures under certain loading and boundary conditions. Later, Fairbairn et al. (2005) also used the smeared crack method to predict the expansion of a concrete dam. Saouma and Perotti (2006) considered the effects of stress state on the ASR expansion of concrete assuming that relatively high compressive or tensile stresses inhibit ASR expansion due to the formation of microcracks and macrocracks that absorb the expanding gel. Multon and Toutlemonde (2006) investigated the effects of moisture distribution and stress state on the ASR-induced expansion in concrete. Comi et al. (2009) created a chemo–thermo-damage model by combining the reaction kinetics and isotropic damage model. Bangert et al. (2004) developed an ASR chemo-hygro-mechanical model by defining three interacting components: the skeleton, the pore liquid and the pore gas in the porous media. Poyet et al. (2007) proposed another law of reaction kinetics for modeling ASR expansion considering the influence of water and temperature.

In the following sections, the ASR swelling model is briefly reviewed. Then, the behavior of a concrete model in LS-DYNA (Hallquist 2006) is evaluated for the purposes of this study. Later, the modeling of the dry cask storage structure is introduced and tip-over event is simulated for the intact and degraded concrete outerpacks. The paper concludes with a discussion of the results and possible future studies.

2. Finite Element Modeling

2.1 Material Models
2.1.1 Alkali-Silica Reaction (ASR) Swelling Model
This paper uses the first order kinetic approach to calculate degradation due to ASR for concrete outerpack which is based on Ulm et al. (2000) and Saouma and Perotti (2006) and the experimental work by Larive (1998). A brief summary of this method is provided in this section. Further details are available in Champiri et al. (2018).

Ulm et al. (2000) stated that the first order ASR kinetics can be represented as

$$1 - \xi = t_c(\xi, \theta)\frac{d\xi}{dt} \tag{4}$$

where ξ is the extent of the ASR reaction ranging from 0 (initial state) to 1 (fully developed), θ is the temperature, and t_c is the characteristic time of the reaction.

With some minor manipulations of Ulm et al. (2000) model, Saouma and Perotti (2006) showed that $t_c(\xi, \theta)$ can be obtained as

$$t_c(\xi, \theta) = \tau_c(\theta)\lambda(\xi, \theta) \tag{5}$$

where

$$\lambda(\xi, \theta) = \frac{1 + \exp\left[-\frac{\tau_L(\theta, I_\sigma, f_c')}{\tau_c(\theta)}\right]}{\xi + \exp\left[-\frac{\tau_L(\theta, I_\sigma, f_c')}{\tau_c(\theta)}\right]} \tag{6}$$

in which I_σ is the first invariant of the stress tensor, f_c' is the compressive strength of concrete, and $\tau_L(\theta, I_\sigma, f_c')$ and $\tau_c(\theta)$ are two time constants of the ASR kinetics, and can be calculated based on the following equations:

$$\tau_c(\theta) = \tau_c(\theta_0) \exp\left[U_C\left(\frac{1}{\theta} - \frac{1}{\theta_0}\right)\right] \tag{7}$$

and

$$\tau_L(\theta, I_\sigma, f_c') = f(I_\sigma, f_c')\tau_L(\theta_0) \exp\left[U_L\left(\frac{1}{\theta} - \frac{1}{\theta_0}\right)\right] \tag{8}$$

in which θ_0 is the reference temperature. Using the Arrhenius equation, the slopes U_C and U_L can be considered as activation energy constants of the characteristic time τ_c and the latency time τ_L, respectively, and Larive (1998) proposed the following ranges based on experimental studies:

$$U_C = 5400 \pm 500 \text{ K} \tag{9}$$
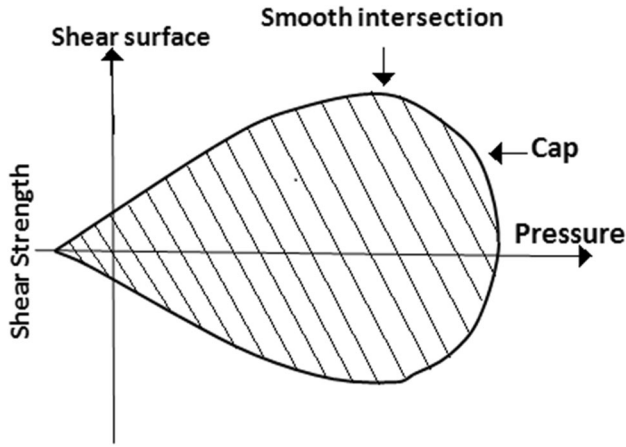
Fig. 1 Failure surface of the CSCM material model.

$$U_L = 9400 \pm 500 \text{ K} \tag{10}$$

The function $f(I_\sigma, f_c')$ represents the effect of compressive stress on the ASR reaction kinetics and can be calculated as:

$$f(I_\sigma, f_c') = \begin{Bmatrix} 1 & \text{if } I_\sigma > 0 \\ 1 + \alpha \frac{I_\sigma}{3f_c'} & \text{if } I_\sigma \leq 0 \end{Bmatrix} \tag{11}$$

$$\text{where } I_\sigma = \sigma_I + \sigma_{II} + \sigma_{III}$$

where σ_I, σ_{II}, σ_{III} are principal stresses. Saouma and Perotti (2006) investigated the effect of volumetric stress on the parameter α in Eq. (11). Equation (11) shows that there is no effect of tensile stress on the reaction kinetics.

Equation (4) is a nonlinear ordinary differential equation that can be solved implicitly using Newton–Raphson iteration of Euler backward integration according to

Table 1 The CSCM material parameters calibrated based on experimental data (Mousavi et al. 2016).

Parameters	Symbols	Values
Shear surface constant term under compression	α	14.2 MPa
Shear surface exponent under compression	β_0	0.01929 MPa^{-1}
Shear surface nonlinear term under compression	λ	10.51 MPa
Shear surface linear term under compression	θ	0.2965
Shear surface constant term under tension	α_1	0.7473
Shear surface exponent under tension	β_1	7.25×10^{-2} MPa^{-1}
Shear surface nonlinear term under tension	λ_1	0.17
Shear surface linear term under torsion	θ_1	1.204×10^{-3} MPa^{-1}
Shear surface constant term under extension	α_2	0.66
Shear surface exponent under extension	β_2	7.25×10^{-2} MPa^{-1}
Shear surface nonlinear term under extension	λ_2	0.16
Shear surface linear term under extension	θ_2	1.45×10^{-3} MPa^{-1}
Fracture energy under compression	G_c	10 KPa.cm
Fracture energy under tension	G_T	0.1 KPa.cm
Fracture energy under shear	G_s	0.1 KPa.cm
Maximum plastic volume compaction	W	0.05
Maximum aggregate size	Agg. size	16 mm
Cap aspect ratio	R	5
Softening parameter under compression	B	10–500
Softening parameter under tension	D	0.05–10
Hardening initiation	N_H	0.7
Hardening rate parameter	C_H	999
Initial cap location	X_0	90 MPa
Cap linear shape parameter	D_1	2.5×10^{-4} MPa
Cap quadratic shape parameter	D_2	3.5×10^{-7} MPa^2
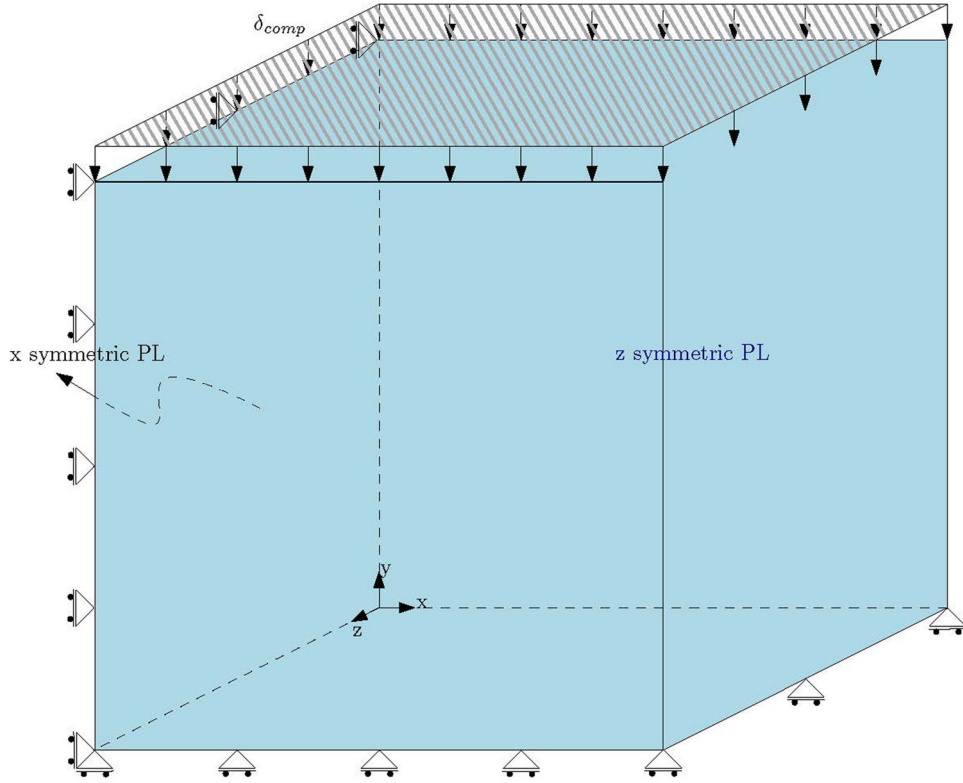
Fig. 2 Boundary and loading conditions for uniaxial compression test (symmetric planes are shown).
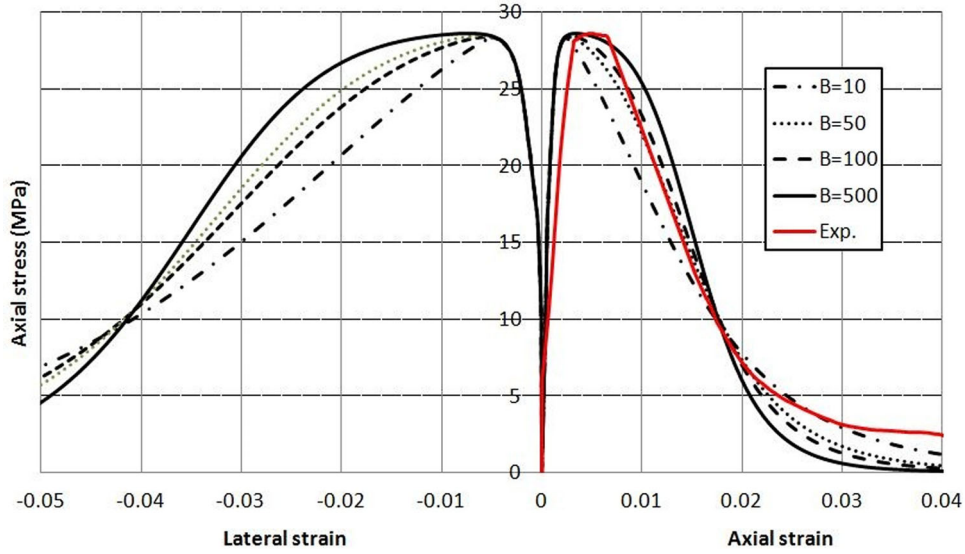
Fig. 3 Comparison of uniaxial compression behavior of CSCM model and experimental data taken from Mousavi et al. (2016).

$$\varphi = \xi_{n+1} - \xi_n - \frac{\Delta t}{\tau_c(\theta_{n+1})_c} \frac{1 - \xi_{n+1}}{\lambda(\xi_{n+1}, \theta_{n+1})} = 0 \qquad (12)$$

where ξ_n and ξ_{n+1} denote the ASR extent at time t_n and $t_{n+1} = t_n + \Delta t$.

After defining the increment of ASR extension, $\Delta \xi$, one can calculate the ASR volumetric strain at each state based on

$$\Delta \varepsilon_{vol}^{ASR} = \Gamma_t \big(f'_t, \ \sigma_I | COD \big) \Gamma_c \big(f'_c, \ \bar{\sigma} \big) g(H) \Delta \xi \varepsilon^\infty \big|_{\theta = \theta_0} \qquad (13)$$

where f'_t denotes the tensile strength of the concrete, and σ_I

is the major principal stress (the positive or the tensile one), COD is the crack opening displacement, $\bar{\sigma}$ is the ratio between the hydrostatic stress and compressive strength of concrete, and ε^∞ is the laboratory-determined maximum free volumetric expansion at the reference temperature θ_0 and it equals to 0.00262 based on Larive (1998). g(H) is a function of relative humidity in concrete, H, and follows

$$g(H) = H^m \qquad (14)$$

where the exponent m is an empirical constant. g(H) has a value between 0 and 1, and here for simplicity it is assumed
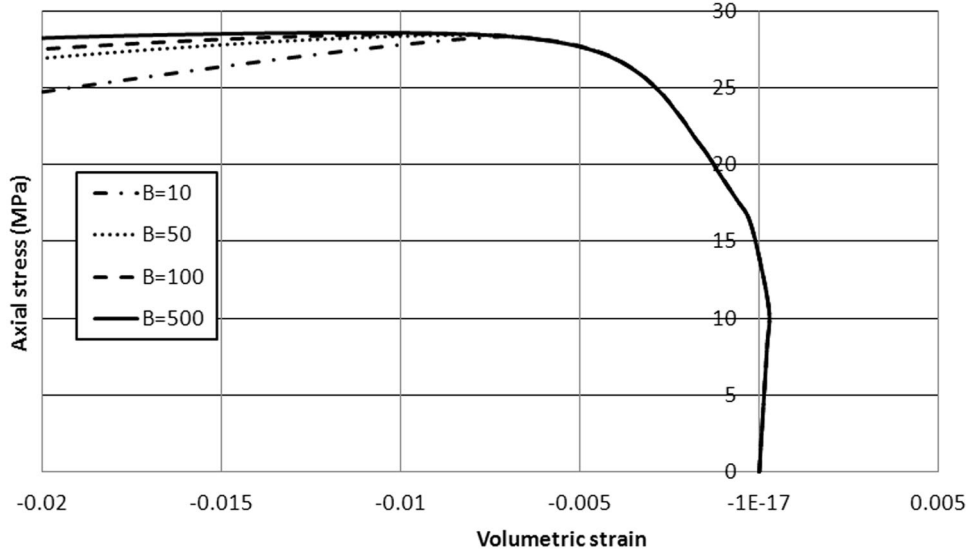
Fig. 4 Compaction to extension behavior of CSCM.
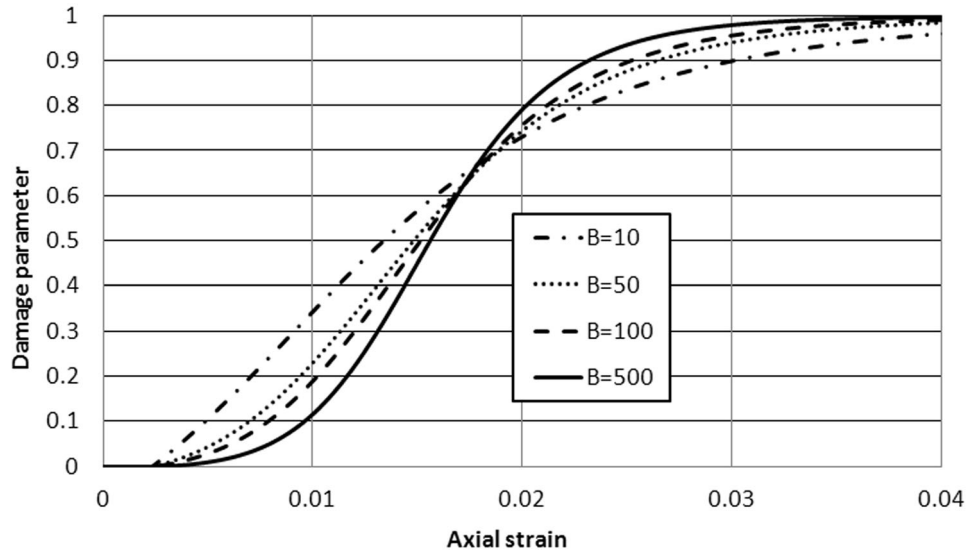
Fig. 5 Compressive damage evolution of CSCM.

equal to 1. The inside temperature for the dry cask structure is considered as 80 °C and the outside temperature is 20 °C in the entire of simulation. The symbol | represents "or" and indicates whether linear elasticity or a smeared crack approach is used. The function $\Gamma_t(f'_t, \sigma_I|\text{COD})$ defines the reduction of ASR expansion due to tensile cracking and it is given by

$$
\Gamma_t
= \left\{
\begin{array}{ll}
\text{Elasticity:} & \left\{\begin{array}{ll} 1 & \text{if } (\sigma_I \leq \gamma_t f'_t) \\ \Gamma_r + (1-\Gamma_r)\frac{\gamma_t f'_t}{\sigma_I} & \text{if } \sigma_I \geq \gamma_t f'_t \end{array}\right\} \\
\text{Smeared crack:} & \left\{\begin{array}{ll} 1 & \text{if } \text{COD}_{max} \leq \gamma_t \omega_c \\ \Gamma_r + (1-\Gamma_r)\frac{\gamma_t \omega_c}{\text{COD}_{max}} & \text{if } \text{COD}_{max} > \gamma_t \omega_c \end{array}\right\}
\end{array}
\right\}
\tag{15}
$$

where γ_t is the fraction of the tensile strength beyond which the gel is absorbed by cracks and is a user input parameter in the simulation. Γ_r is a residual ASR expansion retention factor for ASR under tension, COD_{max} is the maximum

crack opening displacement at the current Gauss point, and ω_c is the maximum COD in the tensile softening curve. Γ_c in Eq. (13) accounts for the reduction in ASR volumetric expansion under compressive stresses and it is given by

$$
\Gamma_c = \left\{
\begin{array}{ll}
1 & \text{if } \bar{\sigma} \leq 0 \text{ tension} \\
1 - \frac{e^{\beta\bar{\sigma}}}{1+(e^\beta-1)\bar{\sigma}} & \text{if } \bar{\sigma} > 0 \text{ compression}
\end{array}
\right\},
$$
$$
\bar{\sigma} = \frac{\sigma_I + \sigma_{II} + \sigma_{III}}{3f'_c}
\tag{16}
$$

where β is an empirical constant (between -2 and 2 according to Samoua and Perroti (2006).

ASR volumetric strain can be calculated with the reported equations and data. ASR strain tensor is built based on this volumetric strain and stress tensor at the time of calculation using weight functions introduced by Saouma and Perotti (2006). The degradation of the modulus of elasticity, E, and tensile strength, f_t, can then be calculated based on
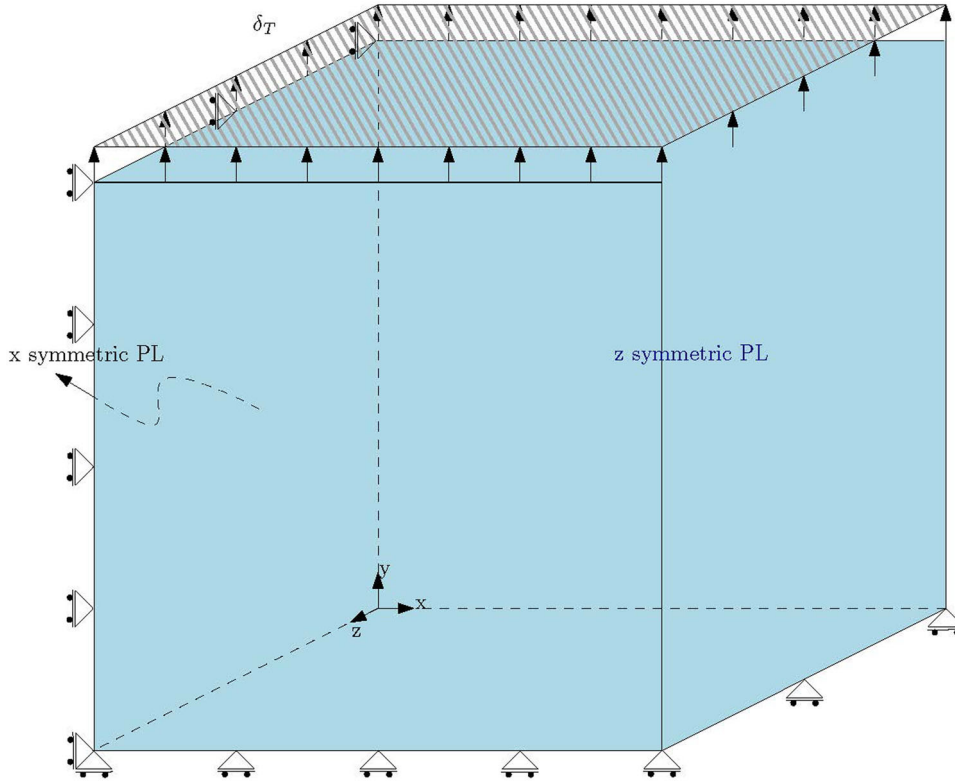
Fig. 6 Boundary and loading conditions for uniaxial tension test.
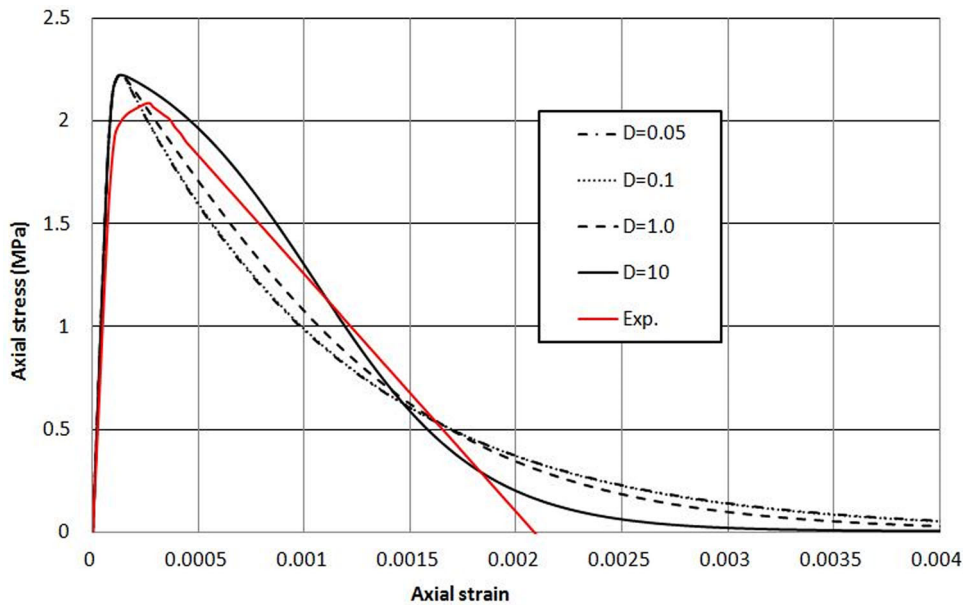
Fig. 7 Comparison of uniaxial tension behavior of CSCM model and experimental data taken from Mousavi et al. (2016).

$$E(t, \theta) = E_0[1 - (1 - \beta_E)\xi(t, \theta)] \qquad (17)$$

$$f_t(t, \theta) = f_{t,0}[1 - (1 - \beta_f)\xi(t, \theta)] \qquad (18)$$

where E_0 and $f_{t,0}$ are the initial elastic modulus and tensile strength, respectively, and β_E and β_f are the corresponding residual fractional values when the concrete has fully reacted.

These functions for elastic modulus and tensile strength are calculated for a fully developed ASR extension where $\xi = 1$, and implemented to the dry cask storage structures

for tip-over contact–impact scenario as described in the following sections.

2.1.2 Continuous Cap Surface Model for Concrete

Several constitutive relationships are available in the materials model library of LS-DYNA (Hallquist 2006). Damage and plasticity are the two important features for a realistic representation of the concrete behavior. The concrete models in LS-DYNA (Hallquist 2006) include Karagozian and Case model (concrete damage model, MAT-72)
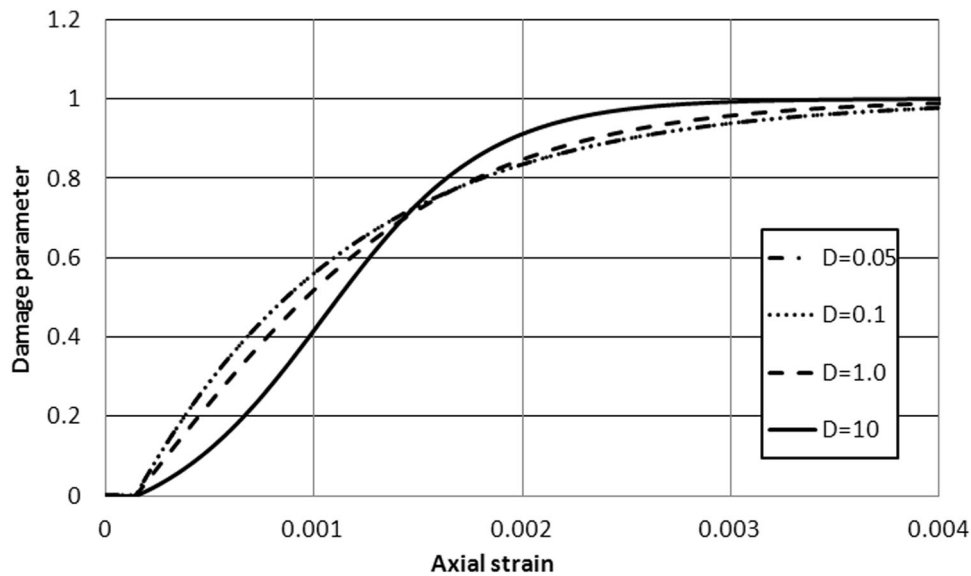
Fig. 8 Tensile damage evolution of CSCM.
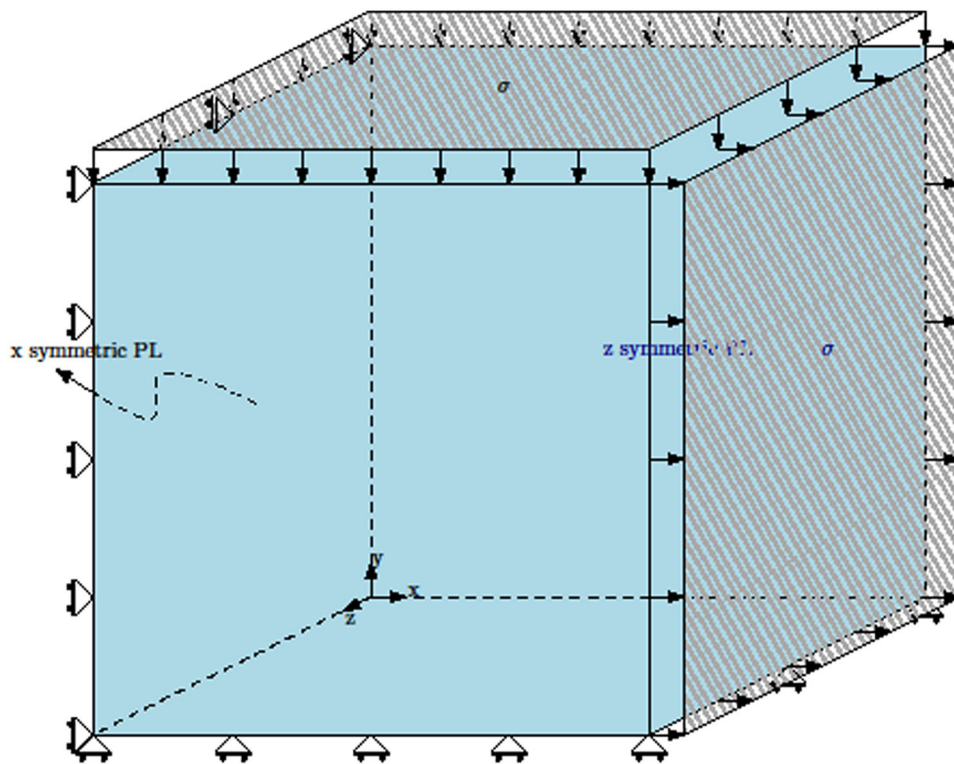
Fig. 9 Boundary and loading conditions for simple shear.

(Brannon and Leelavanichkul 2009; Malvar et al. 1997), the Riedel–Hiermaier–Thoma model (MAT-272) (Borrvall and Riedel 2011; Hansson and Skoglund 2002), the Brannon–Fossum model (Fossum et al. 2004), and the continuous surface cap model (CSCM, MAT-159) (Murray 2007). Among these, CSCM has many applications in the literature (Bermejo et al. 2011; Champiri et al. 2015a, b, 2016; Farage et al. 2004; Mousavi et al. 2016) as it uses only two parameters: uniaxial compressive strength and maximum size of aggregate in the simplest version while other material models need many input parameters. CSCM uses the Duvaut–Lions formulation (Simo et al. 1988) and it is a cap

model with a smooth or continuous intersection between the failure surface and the hardening cap. The yield surface uses a multiplicative formulation to combine the shear (failure) surface with the hardening compaction surface (cap) smoothly and continuously. The smooth intersection eliminates the numerical complexity of treating a compressive "corner" region between the failure surface and the cap as shown in Fig. 1. This type of model is often referred to as a smooth cap model or as a CSCM. Additionally, the rate effects are modeled with viscoplasticity. Since the user cannot control the full behavior of material model (softening, hardening, plasticity and damage) in the simplest version,
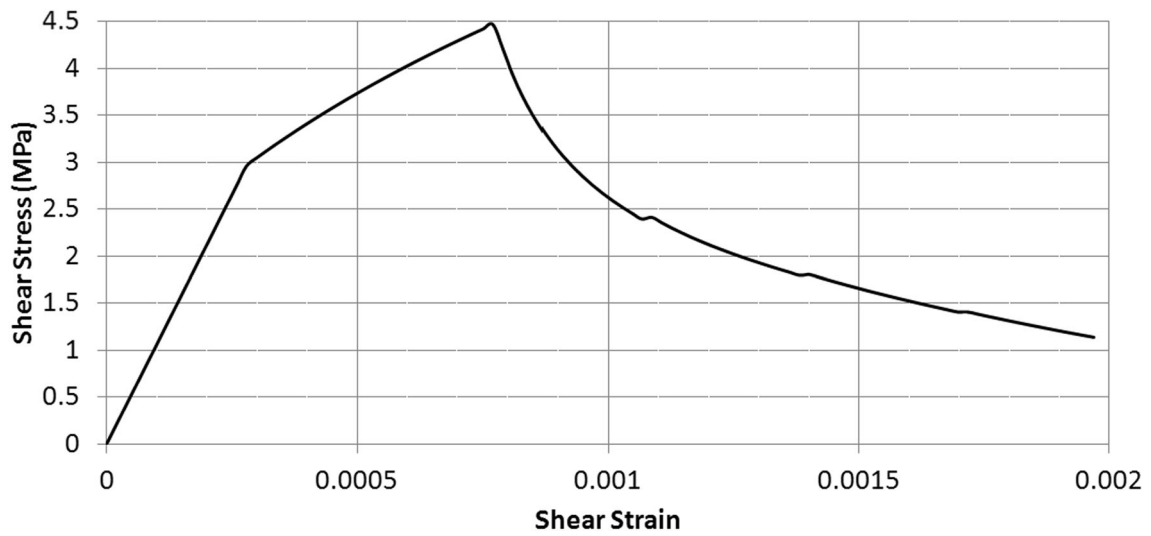
Fig. 10 Simple shear results of CSCM.
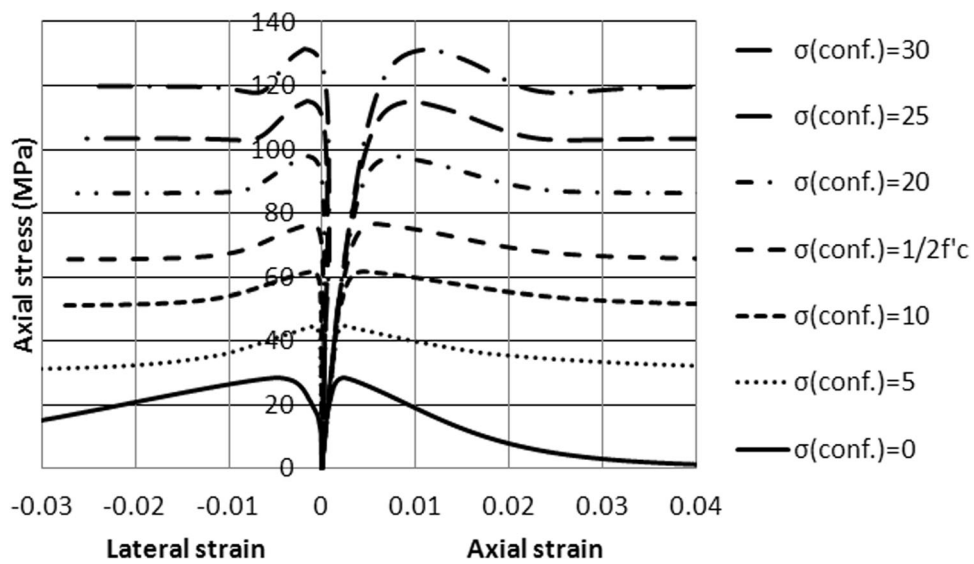
Fig. 11 Effect of confinement on compressive behavior of CSCM material model.
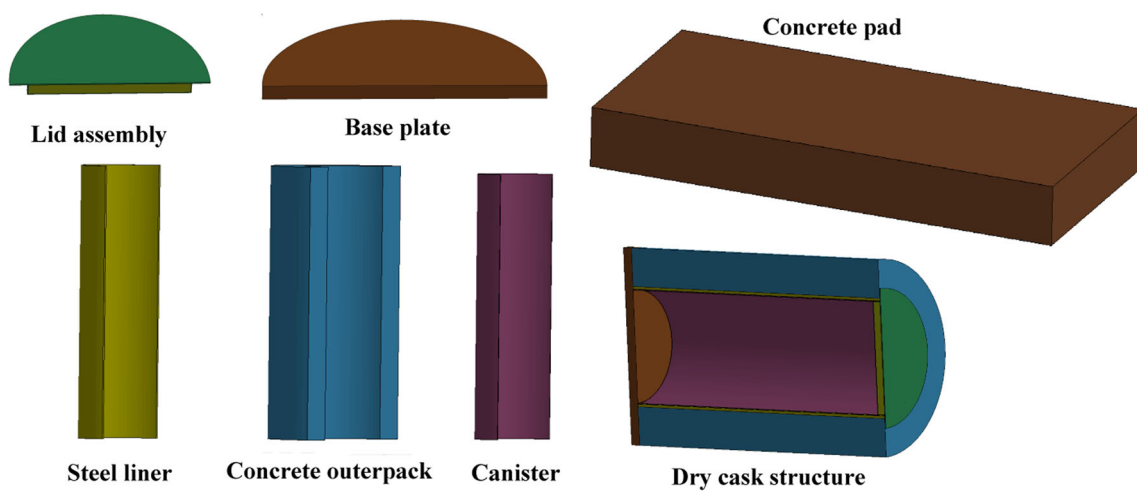
Fig. 12 Different parts of the cask.

Table 2 Dimensions of 1/3-scale cask used in tip-over impact simulations.

Part	Height (mm)	Length (mm)	Width (mm)	Internal radius (mm)	External radius (mm)	Thickness (mm)
Rectangular concrete pad	381.0	3810.0	3810.0	–	–	–
Subgrade soil	2540.0	5080.0	5080.0	–	–	–
Steel liner	1962.2	–	–	355.6	371.5	15.9
Outerpack concrete cask	1962.2	–	–	371.5	609.6	238.1
Lid-top	–	–	–	–	431.8	6.4
Lid-bottom	–	–	–	–	352.4	3.2
Lid-rib	50.8	–	–	349.3	352.4	3.2
Concrete lid	50.8	–	–	–	349.3	349.3
Base plate	–	–	–	–	609.6	63.5
Canister	1905.5	–	–	349.3	352.4	3.2

Table 3 Steel properties for tip-over simulation.

Properties	Values
Density	7850 kg/m^3
Young's modulus	206×10^3 MPa
Poisson's ratio	0.26
Initial yield stress	250 MPa

Table 4 Concrete properties for tip-over simulation.

Properties	Values
Density	2450 kg/m^3
Young's modulus	31×10^3 MPa
Poisson's ratio	0.15
Uniaxial tensile strength	4.3 MPa
Uniaxial compressive strength	41.4 MPa
Biaxial compressive strength	55 MPa

the general version is used in this paper, which needs 44 coefficients. A parameter study is performed here to investigate the behavior of this material model under uniaxial compression, uniaxial tension and simple shear. The set of inputs for the material are given in Table 1. In addition to the compressive fracture energy, there is another parameter called softening under compression, B which controls the post peak regime of the compressive behavior of concrete (see Table 1 for values). Similarly, the parameter which shapes the post peak behavior of concrete under tensile loading condition is, D, along with the tensile fracture energy. The material model was assigned to a single cube element with displacement boundary conditions on the top and symmetric boundary conditions on the two perpendicular sides (see Fig. 2). Roller supports, restraining the

bottom of the element from moving in the load direction, were applied. Concrete shows strain hardening before reaching the maximum strength in compression. Hardening parameters, N_H and C_H, are not clearly investigated for CSCM material model. After calibrating this material model with experimental data (Mousavi et al. 2016), the values shown in Table 1 were proposed.

The analysis was implemented in LS-DYNA (Hallquist 2006) in the case of uniaxial compression and the results are presented in terms of stress versus strain, stress versus volumetric strain and damage evolution with respect to plastic strain as shown in Figs. 3, 4 and 5. The effect of the parameter, B, on the softening shape of CSCM is also shown.
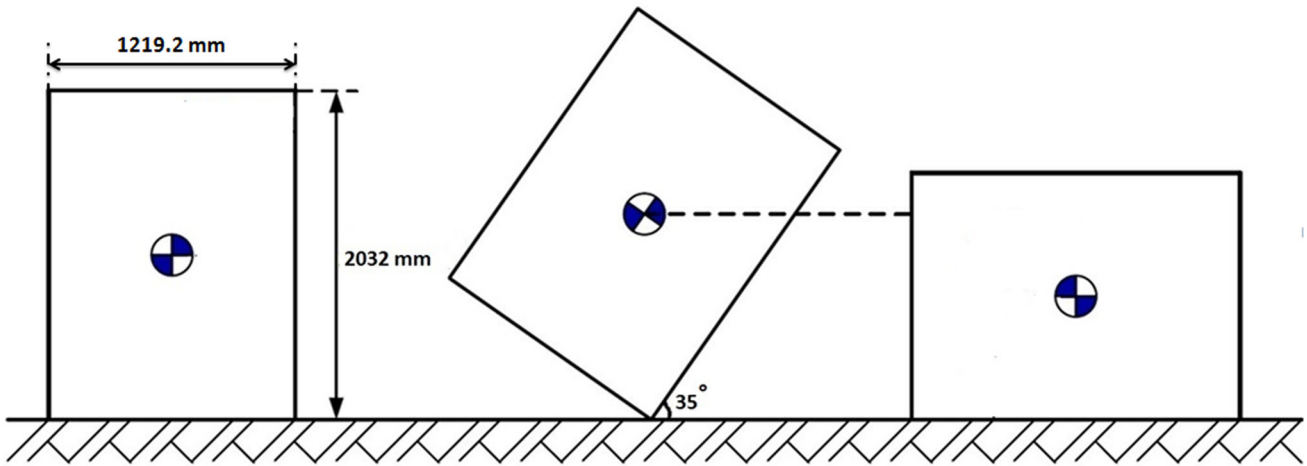
Fig. 13 Positions of the 1/3-scale cask during the tip-over analysis.
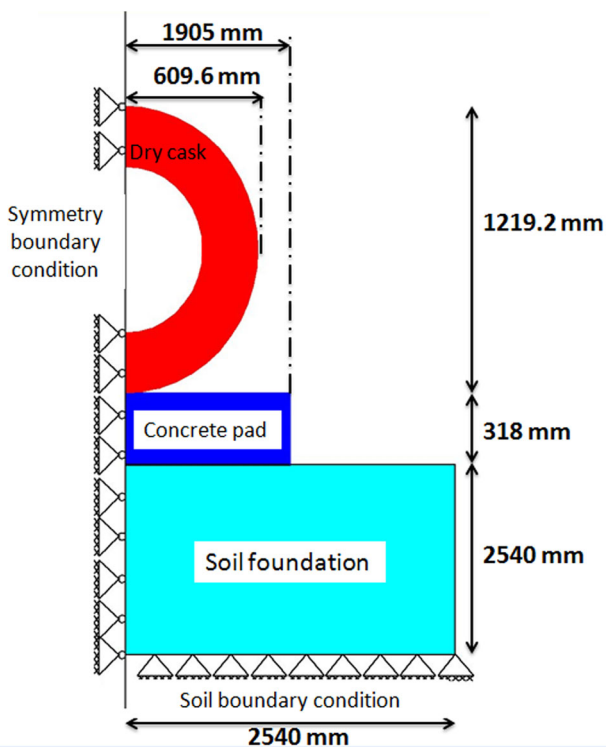
Fig. 14 Boundary conditions for tip-over simulation.

The results of Figs. 3, 4 and 5 show that the model has a realistic behavior. However, it is clearly seen that the lateral strains are too large relative to the experimental data (Mousavi et al. 2016) since this material model uses an associate flow rule. It is expected to observe a higher value of lateral expansion in this material model compared to the experimental data (Mousavi et al. 2016) which was confirmed from the analysis results. The value of 100 was selected for parameter B for further analysis which matches with the experimental data.

The tensile behavior of this material model under monotonic loading was also investigated. The boundary and loading conditions are shown in Fig. 6. Figures 7 and 8 show the behavior of CSCM under uniaxial tension. Additionally, the effect of parameter D on the softening of CSCM

can be seen these figures. The value of 1.0 was selected for parameter D for further analysis which matches with the experimental data,

The performance of CSCM under simple shear was also studied. The boundary and loading conditions are shown in Fig. 9. Figure 10 shows the behavior of CSCM under simple shear. The material model behaves elastic until 3 MPa, then it goes to the hardening regime and maximum shear strength is 4.5 MPa, ultimately it softens as shown in Fig. 10.

The behavior of the model under different confinement levels is presented in Fig. 11. As seen, this material model can predict a realistic behavior under low levels of confinement in the range of compressive strength of concrete. When the level of confinement increases, the strength of the material was increased largely. With 30 MPa confinement, which is around the compressive strength of concrete in the uniaxial compression test, the compressive strength reached to 130 MPa comparable to the experimental data (Montoya et al. 2006).

2.2 Geometry, Boundary Conditions and Meshing

A 1/3-scale dry cask structure was selected to perform tip-over simulation which was referred to in the literature (Champiri et al. 2015a, b, 2017; Hanifehzadeh et al. 2017). The scaled down dry cask structure shows the same behavior as the prototype cask with added mass when dynamic similitude is applied (Champiri et al. 2017). Dry cask structures are constructed of different parts which include: concrete outerpack, steel liner, base-plate, lid assembly and canister. Figure 12 shows different parts of the cask in this simulation. The geometric properties of the cask are summarized in Table 2. The following assumptions were made here with regards to the modeling of the geometry: air outlet and inlet are not considered in this study; base plate was modeled as a solid cylinder. Equivalent mass density of this cylinder was calculated based on the weight of the actual base plate; and the canister was modeled as a rigid inclusion.

In the FE simulations, only half of model cask was considered due to symmetry. The following assumptions were made: extra weight for dynamic similitude was added to the
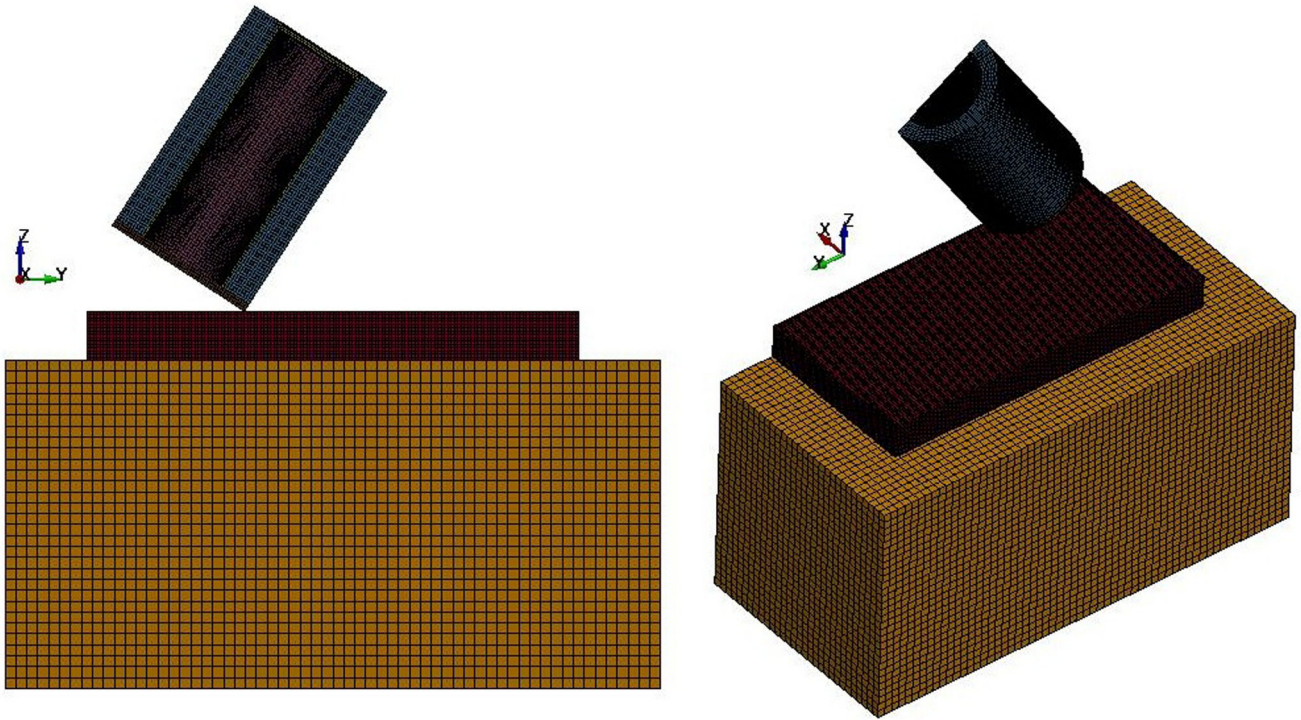
Fig. 15 Initial condition in tip-over simulation for 1/3-scale cask (number of elements = 266,830 and number of nodes = 304,329).
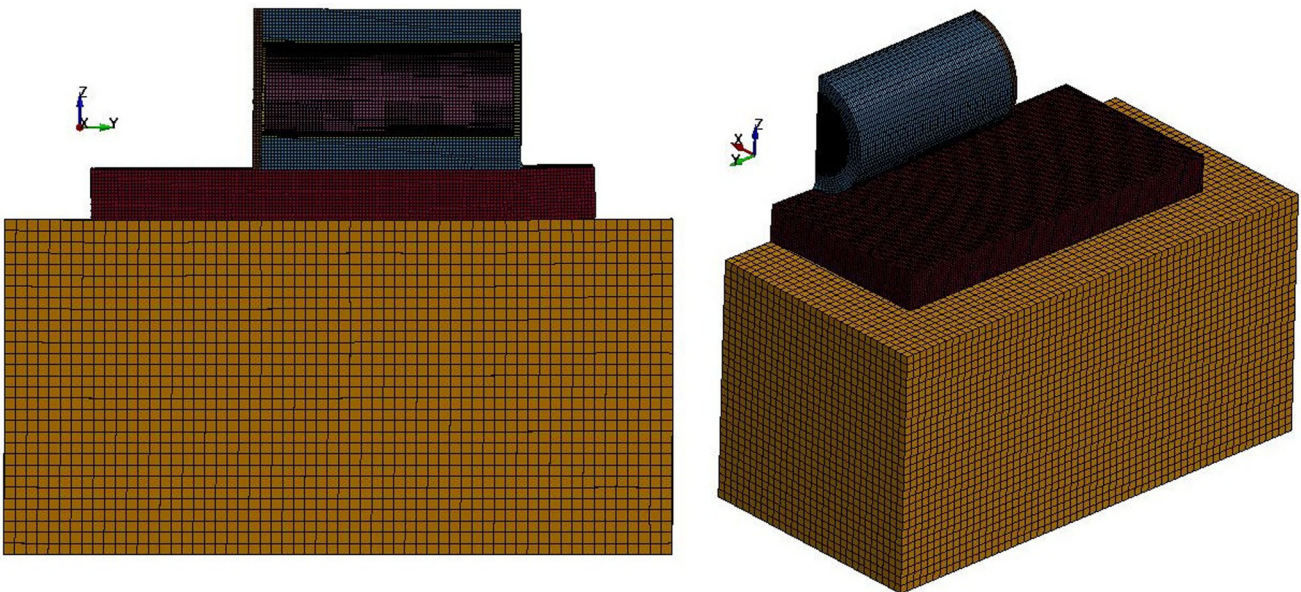
Fig. 16 Impact state in tip-over simulation for 1/3-scale cask.

concrete part by increasing the mass density of concrete; all of cask parts were connected using master–slave type contact (penalty method); isotropic elastic–plastic material model was used for steel; and CSCM was used for the cask and pad concrete. The properties of the steel and concrete are given in Tables 3 and 4, respectively. Isotropic elastic material behavior was assumed for the soil foundation. The modulus of elasticity, Poisson's ratio, and density of soil were taken as 34,500 MPa, 0.3, and 1.5×10^{-4} g/cm^3, respectively (Raheem and Joshaghani 2016; Raheem et al. 2017).

The cask is tilted to 35° as an initial condition (see Fig. 13). Surface to surface contact was used for concrete cask–pad, pad–soil, base plate–pad, canister–base, and canister–liner interfaces. Static and dynamic friction coefficients in the contact surfaces were taken equal to $\mu = 0.3$ for contact between steel parts and $\mu = 0.45$ for contact between concrete and steel parts (Funk 1989). For contact between the cask, steel liner and the lid, tied contact surface-to-surface offset was used to activate penalty method instead of constraint method. Penalty method was found to show less penetration between slave and master, and less mesh

Table 5 Failure criteria in literature for concrete in LS-DYNA (Hallquist 2006).

Problems	Materials	Criteria	Limits	Mesh sizes (mm)	References
Impact	Concrete 27.5 MPa	Principal strain	0.003	$80 \times 80 \times 60$	Huang and Wu (2009)
Blast	Concrete 40 MPa	Principal strain	0.01	$18.75 \times 18.75 \times 25$	Xu and Lu (2006)
Blast	Concrete 24 MPa	Principal strain	0.15	50	Shi et al. (2010)
Blast	Concrete 24 MPa	Shear strain	0.9	50	Shi et al. (2010)
Blast	Concrete 60 MPa	Tensile strain	5 MPa	6.25–100	Tang and Hao (2010)
Blast	Concrete 60 MPa	Principal strain	0.1	6.25–100	Tang and Hao (2010)
Blast	Concrete 40 MPa	Maximum strain	0.1	50	Wu et al. (2011)
Blast	FRC 1% 28 MPa	Shear strain	0.4		Wang et al. (2009)
Blast	FRC 1% 28 MPa	Tensile stress	5.4 MPa		Wang et al. (2009)
Blast	FRC 1.5% 30 MPa	Shear strain	0.4		Wang et al. (2010)
Blast	FRC 1.5% 30 MPa	Tensile stress	6 MPa		Wang et al. (2010)
Blast	FRC 2% 32 MPa	Shear strain	0.4		Wang et al. (2010)
Blast	FRC 2% 32 MPa	Tensile stress	7.5 MPa		Wang et al. (2010)
Blast	FRC 45 MPa	Damage	0.99	25×25	Coughlin et al. (2010)
Dynamic	Concrete 35 MPa	Principal strain	0.002	6–8	Tu and Lu (2010)
Impact	Concrete 40 MPa	Strain limit	1.5		Tu and Lu (2010)
Impact	Concrete 48–140 MPa	Strain failure	−1 (Comp) 0.5 (Tens)	2	Islam et al. (2011)
Impact	FRC 28–32 MPa	Tension stress failure	5.4 MPa	1.25	Teng et al. (2003)
Impact	FRC 28–32 MPa	Shear strain	0.4	1.25	Teng et al. (2003)
Impact	HPFRC	Ultimate shear strain	0.012	6×8	Farnam et al. (2010)

hour glassing in most cases than constraint method while both methods have similar computational cost (www.LS-DYNA-online.com). Penalty method consists of placing normal interface springs between all penetrating nodes and contact surfaces. A force modulus is computed for each slave and master segment based on the thickness and bulk modulus of the element in which it resides. This method results in less mesh hourglassing as compared to the other methods. The time step, Δt, is unaffected by the existence of the interface since the interface stiffness is chosen to be approximately the same order of magnitude as the stiffness of the interface elements.

Friction phenomena exist whenever contacts occur. Friction may play an important role. Classical friction laws (linear dry friction) and non-classical friction laws (e.g., elasto-plastic friction) exist for modeling friction. Classical friction law has physical deficiencies since it allows small relative motion of two contacting bodies even if the friction force is less than $\mu_s N$, where μ_s is the coefficient of static friction, and N is the normal force. The classical friction law ignores the dependence of friction coefficient on the relative sliding velocity. This dependency is significant when the relative sliding velocity is large. The actual coefficient of friction $\mu_c = \mu_d + (\mu_s - \mu_d)e^{-dc.v}$ is assumed to depend on μ_s, μ_d, and dc, where μ_d is the coefficient of dynamic

friction, dc is the exponential decay coefficient and considered to be 0 in this paper, and v is the relative velocity of the surface in contact and equal to $v = \frac{C_1 C_0}{\Delta t}$ where C_1, C_0 are the coordinates of slave node and contact point on the master segment. If exponential decay $dc = 0$ then $\mu_c = \mu_s$ and $f = \mu_s N$.

Internal and external forces are summed at each nodal point, and a nodal acceleration is computed by dividing by nodal mass. The solution is advanced by integrating this acceleration in time. The maximum time step is limited by the Courant condition, producing an algorithm which typically requires many relatively inexpensive time steps.

The displacement component in the circumferential direction of the nodes in the plane of symmetry was restrained. During the tip-over event, only the responses within near field of the soil foundation are of interest and stress waves should not be reflected (Raheem and Joshaghani 2016; Raheem et al. 2017). Thus, a thick layer of soil was considered so that the stress waves are not reflected. Figure 14 shows the boundary conditions of the tip-over simulation.

A fine mesh was used for tip-over simulation. Eighty elements were specified along the length of the concrete outerpack. As a result, each element had a size of 25 by 25
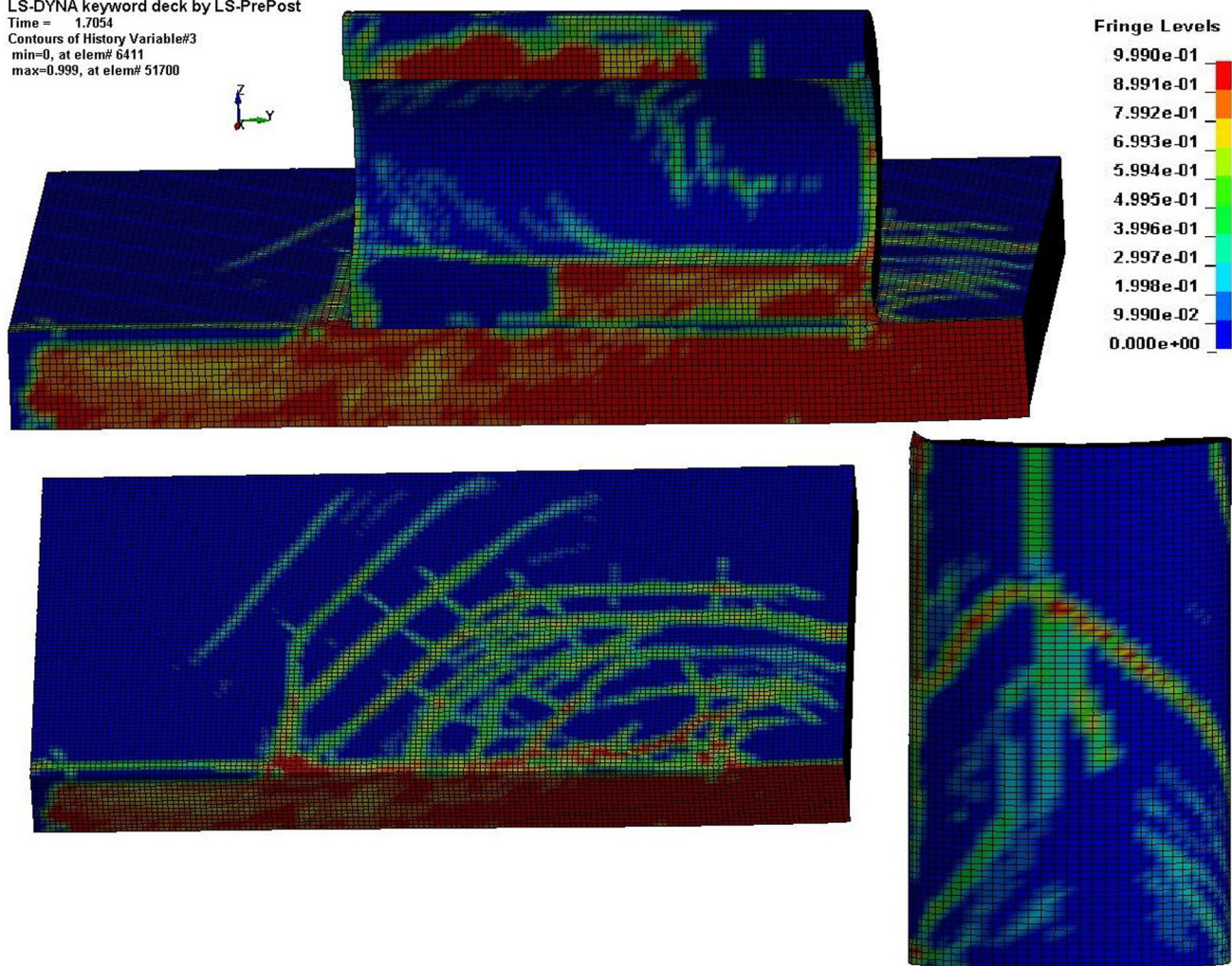
Fig. 17 Contours of ductile damage at t = 1.7054 s.

2.3 Solution Techniques and Assessment Metrics

Hourglass mode was considered using the Belytschko–Bindeman (1993) formulation of assumed strain co-rotational stiffness form for 2D and 3D solid elements with one integration point. This form is available for explicit problems in LS-DYNA (Hallquist 2006). Hourglass energy, which is the work done by the forces calculated to resist the hourglass modes, was removed from the physical energy of the system. Hourglass energy was taken acceptable when it is less than 10% of the total energy (www.LS-DYNA-online.com). Sliding interface energy or contact energy is another important issue in this problem. This energy should not be less than zero to satisfy the definition of the contact. In addition, it is recommended that this number should be less that 10% of the total energy (www.LS-DYNA-online.com). Rate effects should also be considered in impact–contact type problems. Therefore, the rate sensitivity of concrete was considered here for the CSCM (Murray 2007).

The internal time step of this analysis was $4.45E^{-08}$ s. This small number was chosen by LS-DYNA (Hallquist 2006) software because of explicit time integration of two-body contact and to properly apply the penalty method within the convergence limits. This simulation takes 2 days to complete using eight processors in parallel. Contact happened at time equal to 1.6482 s (corresponding to the maximum acceleration at tip of the cask) after starting tip-over simulation from initial condition at 35° tilt. Figures 15 and 16 show the simulation at initial state and after impact by LS-DYNA (Hallquist 2006) software.

Elements can be deleted in LS-DYNA when they reach a failure criterion using MAT-ADD-EROSION option. Different failure criteria can be introduced with this keyword based on maximum principal strain, maximum shear strain, pressure, principal stress, and damage. In the literature, mostly, principal strain and shear strain were used for concrete structures. Some researchers also used tensile damage and tensile stress for evaluation of failure. An extensive literature review was performed here in order to find a suitable failure criterion for tip-over impact of concrete casks in LS-DYNA (Hallquist 2006). Table 5 summarizes each work based on the mesh, failure criteria and type of the
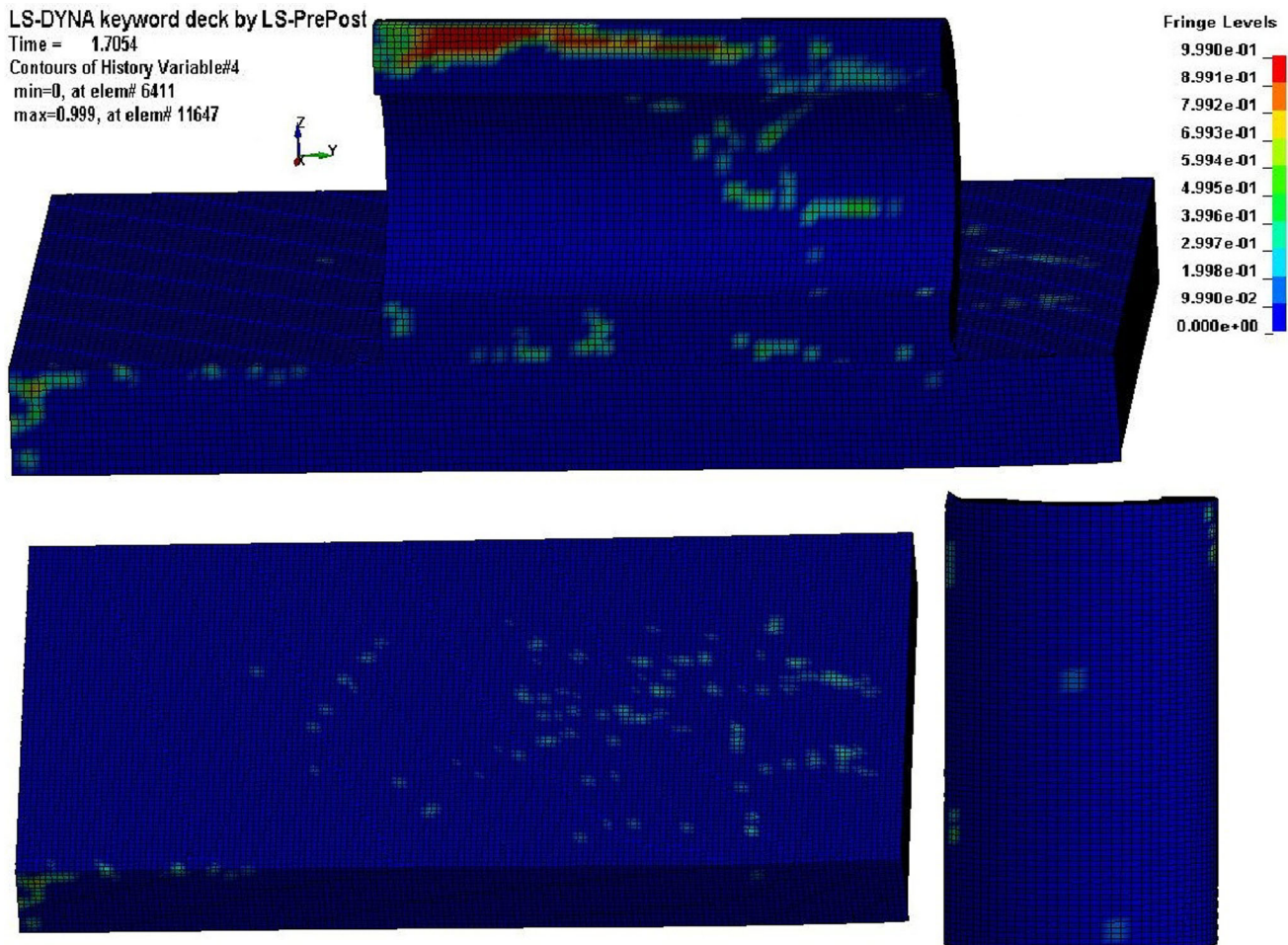
Fig. 18 Contours of brittle damage at t = 1.7054 s.

structural concrete (Coughlin et al. 2010; Farnam et al. 2010; Huang and Wu 2009; Islam et al. 2011; Shi et al. 2010; Tang and Hao 2010; Teng et al. 2003; Tu and Lu 2010; Wang et al. 2009; Wang et al. 2010; Wu et al. 2011; Xu and Lu 2006).

A mesh size of 25 × 25 × 25 mm was used here, which is reasonable based on the literature review. Activating the element erosion algorithm makes the model run faster since some elements were deleted while performing the tip-over simulations.

It was discovered that using only the maximum compressive strength as an erosion criterion is not acceptable because the stiffness of the structure is highly decreased when the element is deleted, in other words, the stiffness of elements in the softening part is neglected. Then, a damage based criterion was tried. A damage parameter of 0.99 was used. However, it was seen that this criterion cannot capture the shear band and shear cracks correctly. Therefore, a combination of damage and maximum shear strain was used. Selecting a value for maximum shear strain is not straightforward and it is highly dependent on the material model. A value between 0.1 and 0.9 was reported in the literature (Coughlin et al. 2010; Morris et al. 2013; Wang et al. 2010; Xu and Lu 2006). It was concluded that a value of 0.1 can

better describe this criterion for CSCM during this contact–impact problem.

3. Results and Discussion

3.1 Tip-Over Analysis of Dry Cask Structure with Intact Concrete

The result of tip-over simulation is presented in this section in the form of contours of ductile damage (a scalar between 0 and 1 indicating the level of compressive damage of elements), contours of brittle damage (a scalar between 0 and 1 indicating the level of compressive damage of elements), contour of von-Mises stress, and acceleration at the tip of cask. Figure 17 shows ductile damage contours in different regions of the 1/3-scale intact cask. It is seen that the pad and edge of the cask in the contact area reach to the maximum ductile damage (0.99). Additionally, the opposite edge of the cask also shows ductile damage. Figure 18 shows the brittle damage contours due to tensile stresses in different regions of the 1/3-scale cask. The outer edge of the cask reaches the maximum brittle damage, while the other regions do not show any critical brittle damage. Figure 19 shows the contours of von-Mises stresses. The contact area
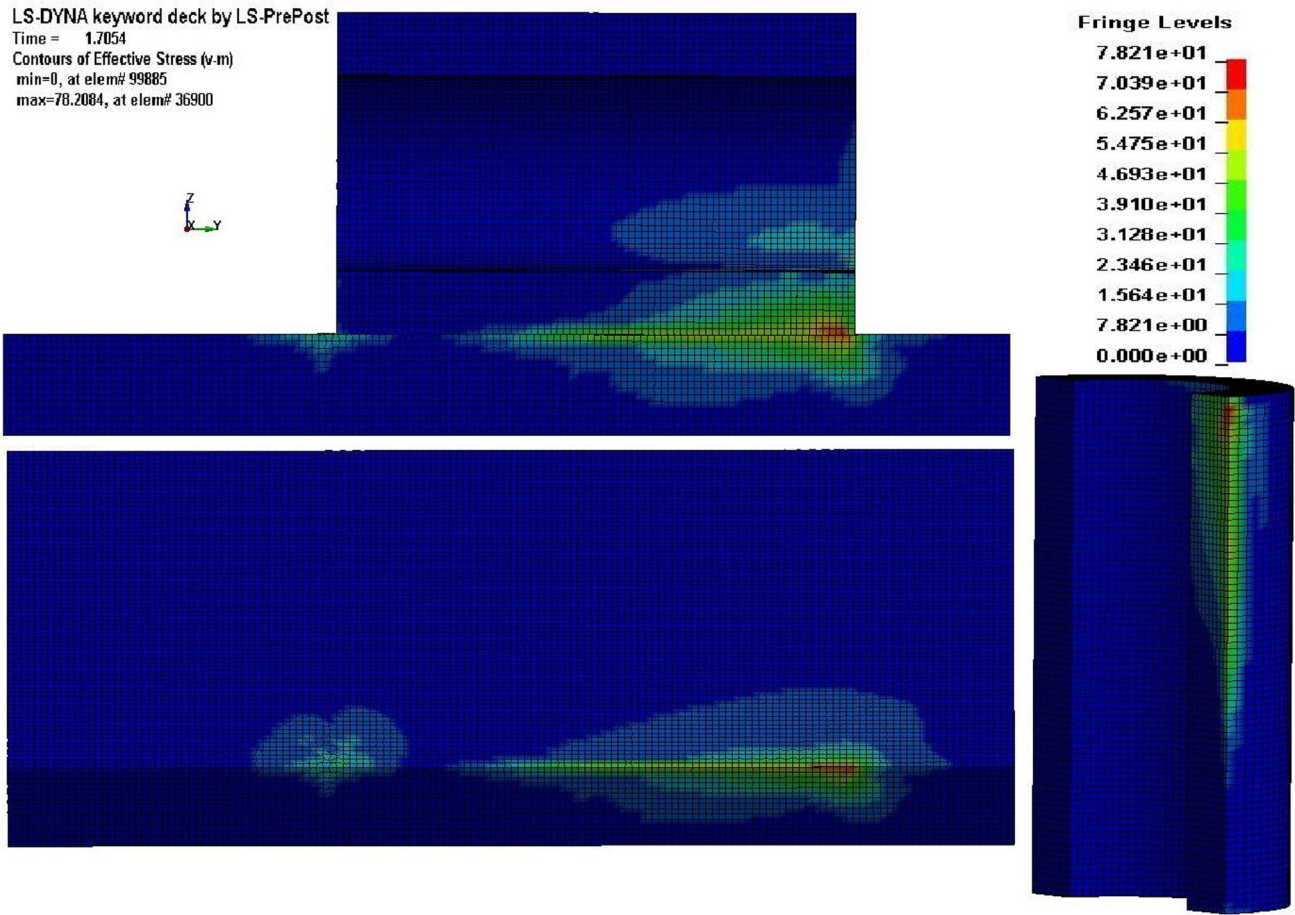
Fig. 19 Contours of von-Mises stress (MPa) at t = 1.7054 s.
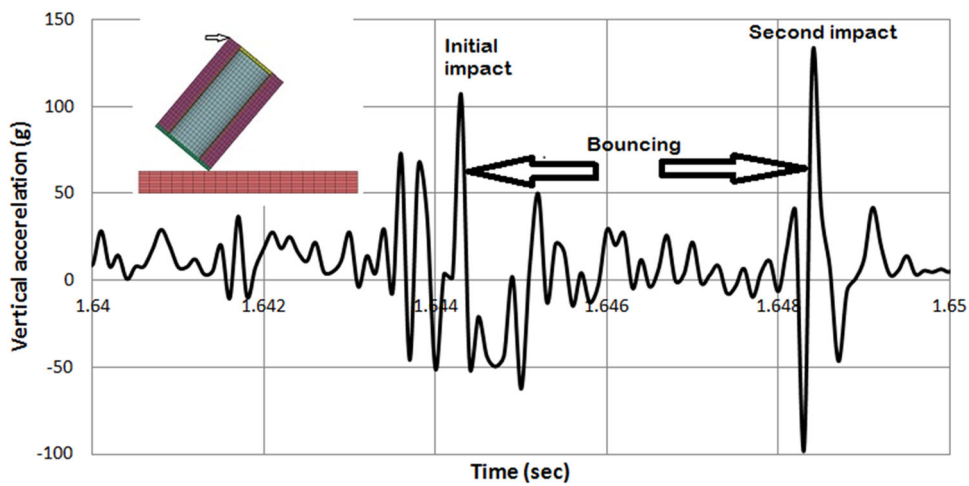
Fig. 20 Time history of vertical acceleration at selected node for the model cask.

reaches the maximum von-Mises stress at 78 MPa which is due to the triaxiality effect.

For numerical damping, global damping was adopted in all models in order to dissipate energy. The past literature recommends 0.5 as a global damping coefficient (LS-DYNA examples manual 2001; Morris et al. 2013). Vertical acceleration time history is shown in Fig. 20. Maximum

acceleration reaches to 150 g at the tip of the cask on the opposite side of the contact area. This maximum acceleration can be verified by experimental studies, however, since the objective of this study is to make a relative comparison between the intact and the ASR affected concrete, and this coefficient is constant for both models, it is believed that the
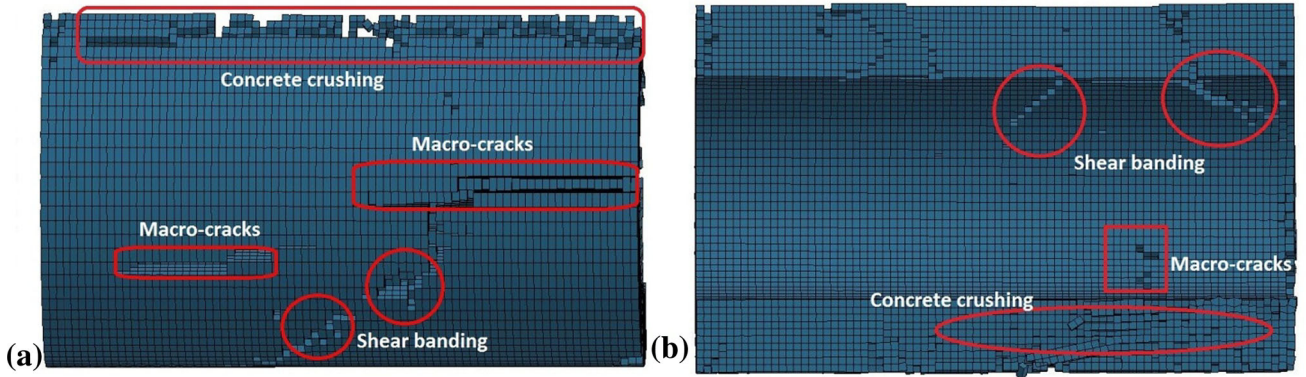
Fig. 21 **a** Inside of the concrete cask and **b** outside of the concrete cask.

(a) inside of the concrete cask

(b) outside of the concrete cask
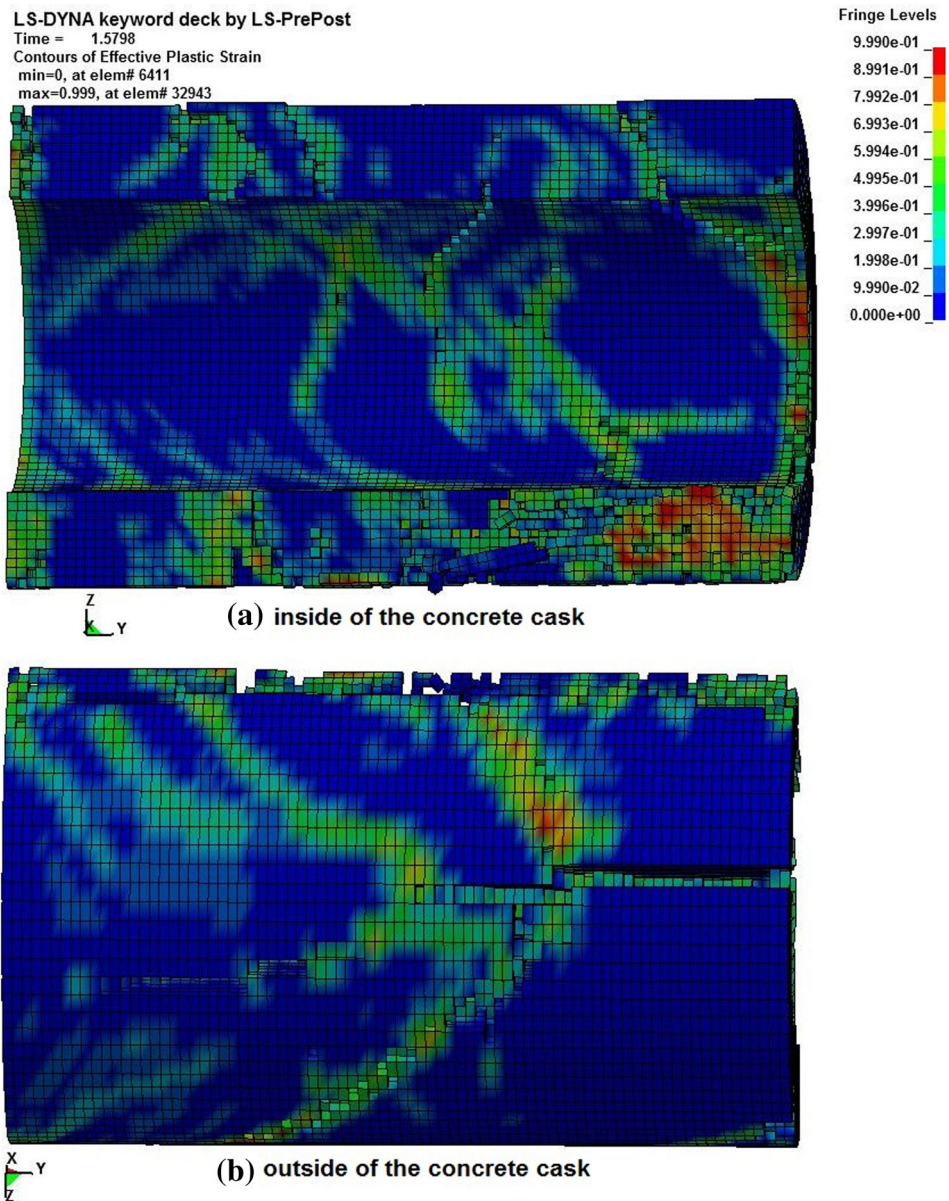
Fig. 22 Maximum brittle and ductile damage contours for the concrete cask.
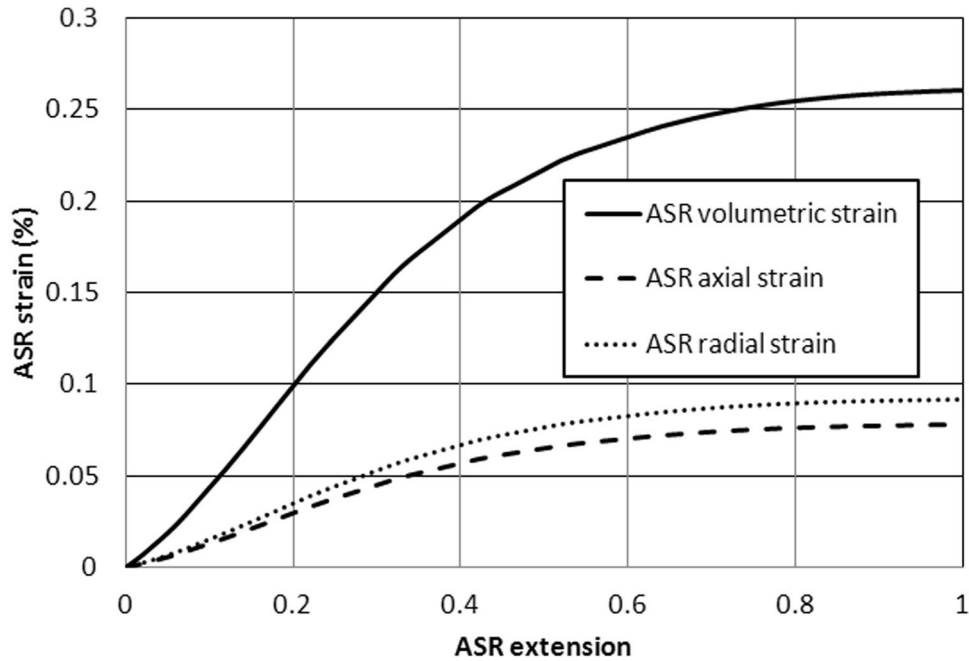
Fig. 23 ASR strains in the concrete outerpack of dry cask structure.

Table 6 Concrete properties for tip-over simulation.

Properties	Values
Density	2450 kg/m^3
Young's modulus	15.5×10^3 MPa
Poisson's ratio	0.15
Uniaxial tensile strength	2.15 MPa
Uniaxial compressive strength	12.5 MPa

exact value of accelerations do not hinder such a comparison.

3.2 Failure Analysis of Tip-Over Analysis of 1:3 Model Dry Cask Structures

In this section, failure modes of the dry cask structure are investigated. The same geometry, boundary and initial conditions, and material properties as for the previous sections were used. The failure criteria described in Sect. 2.3 was adopted.

Figure 21 shows the failure modes of the concrete after impact. As seen in the figure, concrete crushing is significant near the edge on the contact area. Shear banding is dominant near the outer edge of the cask and it is seen both from inside and outside of the cask. Several cracks were observed on the cask especially in the middle body and far from the edges. Figure 22 shows the contours of the absolute value of brittle and ductile damage (whichever amount is greater) in the concrete cask. Red areas in Fig. 22 show the maximum level of damage (brittle or ductile) where the elements are close to be eroded. Damage in the green area is about 0.5 (brittle or ductile). Blue areas remain undamaged during this tip-over simulation. Diagonal propagation of damage shows the

importance of shear failure criteria introduced in the erosion algorithm described above in Sect. 2.3.

3.3 Tip-Over Simulation of Model Dry Cask Using the ASR Affected Concrete

The first order swelling model (Saouma and Perotti 2006; Ulm et al. 2000), which was described briefly in Sect. 2.1, was implemented to determine the level of degradation for a fully extended ASR state in the dry cask structure. COMSOL Multiphysics (2015) was used to model the ASR behavior of dry cask structure. For this purpose, only the concrete outerpack and the steel liner were considered. A 2D axisymmetric model was developed. The stress and strain components were calculated in all directions including axial (z), radial (r), and tangential (θ) directions. Friction was applied between these two parts and the same coefficient of friction with the same value of 0.45 as in the tip-over impact case was used.

The gravity load was applied to the entire model and the outer and upper surfaces of the concrete outerpack had free boundary condition, therefore, initially the stress and strain were zero in the model. In order to capture the degradation of the concrete outerpack, mechanical and environmental effects were evaluated before the tip-over simulation starts.
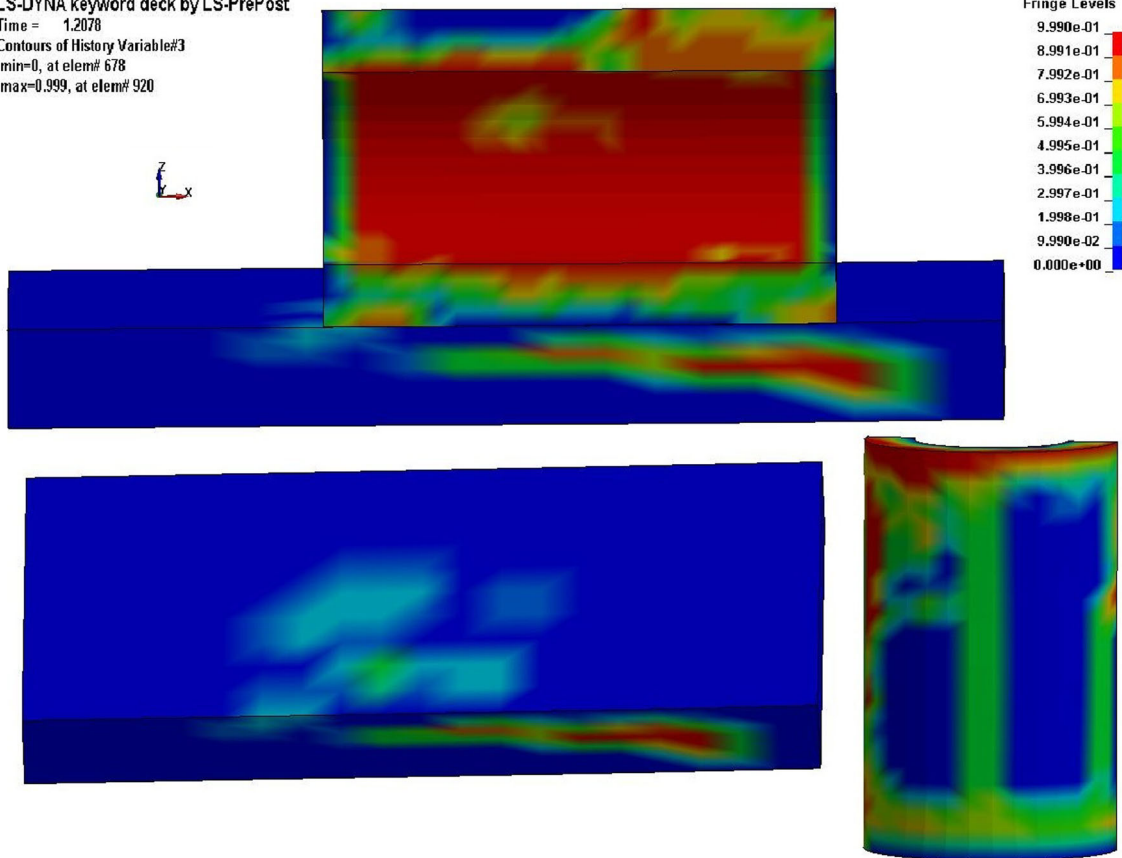
Fig. 24 Contours of ductile damage at the time of impact.
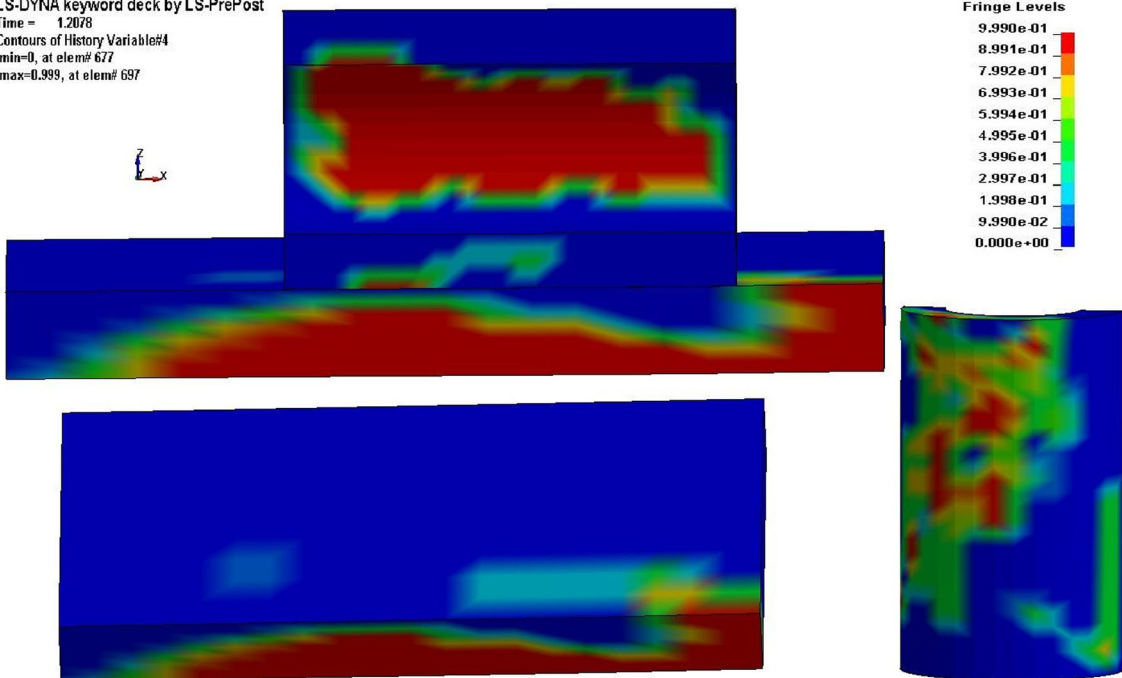
Fig. 25 Contours of brittle damage at the time of impact.
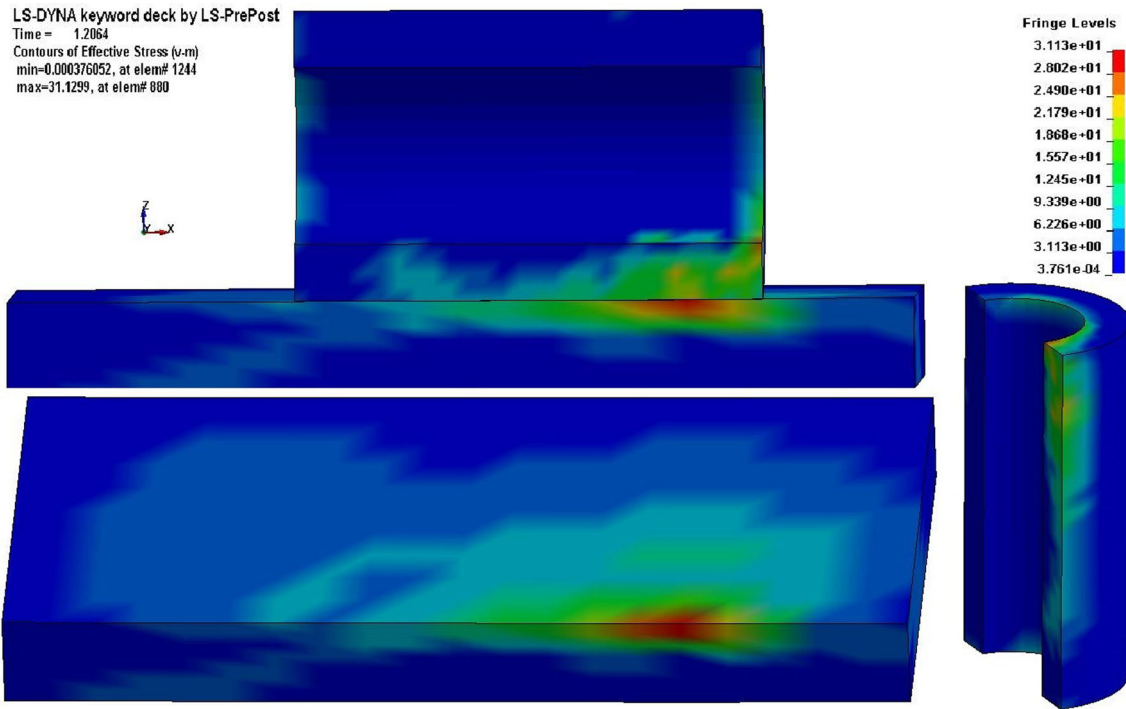
Fig. 26 Contours of von-Mises stress at the time of impact.
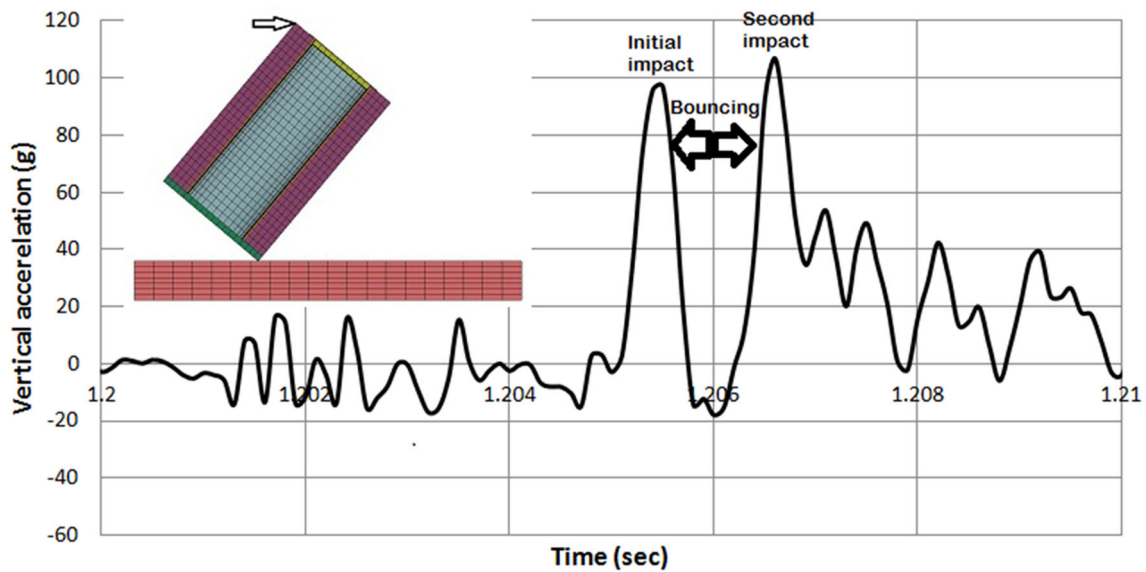
Fig. 27 Time history of vertical acceleration at the tip of the cask.

Environmental effect of degradation was applied to the model through the strain tensor, as ASR induces strains into the concrete part, and because of the confinement, stresses develop in the model. Figure 23 shows the volumetric strain of ASR reaction, ASR axial strain, and ASR radial strain in the concrete part of dry cask structure along with the extension of ASR.

Mechanical degradation was introduced by reducing the modulus of elasticity and tensile strength in the concrete model (Saouma and Perotti 2006). As described earlier, degradation of the modulus elasticity and tensile strength of the concrete cask was calculated based on based on the first

order kinetic approach (Saouma and Perotti 2006) for a fully developed ASR case following

$$
\begin{aligned}
E(t, \theta) &= E_0[1 - (1 - \beta_E)\xi(t, \theta)] \\
&= 31[1 - (1 - 0.5) \times 1.00] = 15.5 \text{ GPa}
\end{aligned} \tag{19}
$$

$$
\begin{aligned}
f_t(t, \theta) &= f_{t,0}[1 - (1 - \beta_f)\xi(t, \theta)] \\
&= 4.3[1 - (1 - 0.5) \times 1.00] = 2.15 \text{ MPa}
\end{aligned} \tag{20}
$$

where E_0 and and $f_{t,0}$ were taken as 31,000 and 4.3 MPa, respectively. β_E and β_f were taken equal to 0.5 based on Saouma and Perotti (2006).

For fully extended ASR, E was obtained to be 15,500 MPa, where it was originally 31,000 MPa. Using the

ACI formulation (2008), Here, the uniaxial compressive strength was calculated as $f'_c = 12.5$ MPa, where it was originally 41.1 MPa. Additionally, the reduced the tensile strength was obtained as $f'_t = 2.15$ MPa

ASR strain was computed in three orthogonal directions based on the first order kinetic model. It was shown that $\varepsilon_r = \varepsilon_\theta = 0.0087$, and $\varepsilon_z = 0.0076$. This initial strain was translated into LS-DYNA (Hallquist 2006) model as initial strains in form of the temperature gradient using different values for the thermal coefficient (α) in each direction.

Isotropic elastic–plastic material model was used for the steel part. CSCM, as introduced earlier, was used for mechanical behavior of the cask concrete and pad. The properties of the degraded concrete are summarized in Table 6.

The internal time step of this analysis was 4.44E−07 s. This simulation took longer than the intact model since strain states were introduced to all the elements of the concrete outerpack. Contact happened at time equal to 1.2078 s (corresponding to the maximum acceleration at tip of the cask) after starting the tip-over simulation from the initial condition.

Figures 24 and 25 show the ductile and brittle damage contours, respectively, in different regions of the 1/3-scale cask. Figure 26 shows the contours of von-Mises stress.

Concrete crushing was observed as the dominant failure mode in this case and it was seen that most regions of the concrete outerpack are fully damaged in both ductile and brittle damage (red regions). Since the concrete is damaged due to ASR, shear banding does not occur at the same extent as for the intact cask. Additionally, it was seen that during this impact, concrete outerpack is divided into two parts through a large crack (see Fig. 24). The von-Mises stresses were reduced in the ASR damaged cask which is an indication that the elements are in the softening regime and they are de-stressed.

Time history of vertical acceleration is shown in Fig. 27. Maximum acceleration was reduced to 100 g. Since the concrete outerpack is not stiff as the previous model, this reduction of the maximum acceleration was expected.

4. Conclusions

In this paper, the behavior of a dry cask structure damaged due to ASR was investigated in the form of damage, failure modes, stresses, and accelerations under a hypothetical tip-over event. First, a study was done which considered the concrete part of the cask in intact condition with full strength and stiffness. Then, a degraded concrete outerpack due to ASR was considered where the environmental and mechanical degradations were calculated using the first order kinetic approach. The following conclusions are made by comparing these two cases:

- It was shown the intact dry cask is locally damaged under this tip-over scenario, where the edge of concrete in the contact zone crushes, and the other edge is

exposed to the shear banding. Several cracks were observed also observed.
- When the ASR is fully developed in the concrete outerpack, a reduction of approximately 50% was observed for the modulus of elasticity and tensile strength.
- Environmental degradation due to ASR was calculated in the form of strain tensor and implemented in LS-DYNA (Hallquist 2006) in the form of temperature gradient before tip-over starts.
- Maximum acceleration at outer edge of concrete reaches to 150 g which reduces to 100 g when the stiffness is reduced due to ASR damage.
- Concrete crushing is the dominant failure mode in the case of fully expanded ASR where damage parameter reaches to 0.99 in the form of brittle damage and ductile damage in the entire structure.
- It was shown that a large crack divides the cask into two parts when the effect of ASR is considered in this hypothetical event.

Open Access

References

ACI 318-08 (2008). *Building code requirements for structural concrete and commentary.* American Concrete Institute.

Bangert, F., Kuhl, D., & Meschke, G. (2004). Chemo-hygromechanical modelling and numerical simulation of concrete deterioration caused by alkali-silica reaction. *International Journal for Numerical and Analytical Methods in Geomechanics, 28*(78), 689–714.

Belytschko, T., & Bindeman, L. P. (1993). Assumed strain stabilization of the eight node hexahedral element. *Computer Methods in Applied Mechanics and Engineering, 105,* 225–260.

Bermejo, M., Goicolea, J. M., Felipe Gabaldon, F., & Santos, A. (2011). Impact and explosive loads on concrete buildings using shell and beam type elements. In *COMPDYN 2011, 3rd ECCOMAS thematic conference on computational methods in structural dynamics and earthquake engineering*, Greece, May 25–28.

Borrvall, T., & Riedel, W. (2011). The RHT concrete model in LS-DYNA. In *Proceedings of the 8th European LS-DYNA users conference*, Strasbourg.

Brannon, R. M., & Leelavanichkul, S. (2009). *Survey of four damage models for concrete*. Sandia National Laboratories, SAND2009-5544.

Champiri, M. D., Attar, A., Hanifehzadeh, M., Willam, K., & Gencturk, B. (2015a). Long-term performance of dry storage structures. In *CONCREEP-10 conference*, September 21–23, Vienna, Austria.

Champiri, M. D., Attar, A., Hanifehzadeh, M., Willam, K., & Gencturk, B. (2015b). Tip-over simulation of degraded dry storage structures. In *Proceedings of the ASME 2015 international mechanical engineering congress and exposition (IMECE15)*, November 13–19, Houston, TX, USA.

Champiri, M. D., Mohammadipour, A., Mousavi, R., Willam, K., & Gencturk, B. (2017). Added mass effect for tip-over analysis of dry cask composite structures at two different scales. *Annals of Nuclear Energy, 110,* 126–139.

Champiri, M. D., Mousavi, R., Hanifehzadeh, M., Attar, A., Willam, K., & Gencturk, B. (2016). Drop test of a thick-walled concrete cylinder subjected to shrinkage and expansion. In *9th International conference on fracture mechanics of concrete and concrete structures*, FraMCoS-9.

Champiri, M. D., Mousavi, R., Willam, K., & Gencturk, B. (2018). *A calibration of alkali-silica reaction model for long-term performance of dry cask storage concrete structures. Nuclear science and techniques*. Berlin: Springer.

Champiri, M. D., Mousavizadegan, S. H., & Moodi, F. (2012). A decision support system for diagnosis of distress cause and repair in marine concrete structures. *International Journal of Computers and Concrete, 9*(2), 99–118.

Comi, C., Fedele, R., & Perego, U. (2009). A chemo–thermo-damage model for the analysis of concrete dams affected by alkali-silica reaction. *Mechanics of Materials, 41*(3), 210–230.

COMSOL Multiphysics® (2015). *The platform for physics-based modeling and simulation*. http://www.comsol.com/comsol-multiphysics.

Coughlin, A., Musselman, E., Schokker, A., & Linzell, D. (2010). Behavior of portable fiber reinforced concrete vehicle barriers subject to blasts from contact charges. *International Journal of Impact Engineering, 37*(5), 521–529.

Dilger, F., Halstead, R. J., & Ballard, J. D. (2012). Full-scale cask testing and public acceptance of spent nuclear fuel shipments-12254. In *WM 2012 conference*, February 26–March 1, Phoenix, AZ, USA.

Dytran (2008). Explicit dynamics and fluid structure interaction: User's guide. MSC Software.

Elfahal, M. M. (2003). *Size effect in normal and high-strength concrete cylinders subjected to static and dynamic axial compressive loads*. PhD Dissertation, The Pennsylvania State University.

Fairbairn, E. M. R., Ribeiro, F. L. B., Lopes, L. E., Toledo-Filho, R. D., & Silvoso, M. M. (2005). Modelling the structural behavior of a dam affected by alkali-silica reaction. *Communications in Numerical Methods in Engineering, 22*(1), 1–12.

Farage, M., Alves, J. L. D., & Fairbairn, E. M. R. (2004). Macroscopic model of concrete subjected to alkali-aggregate reaction. *Cement and Concrete Research, 34*(3), 495–505.

Farnam, Y., Mohammadi, S., & Shekarchi, M. (2010). Experimental and numerical investigations of low velocity impact behavior of high-performance fiber-reinforced cement based composite. *International Journal of Impact Engineering, 37*(2), 220–229.

Fossum, A., Brannon, R., Fossum, A. F., & Brannon, R. M. (2004). *The Sandia geomodel: Theory and users guide*. Sandia National Laboratories, SAND2004-3226.

Funk, R. (1989). Shear friction transfer mechanisms for supports attached to concrete. *American Concrete International Journal, 11*(7), 53–58.

Gupta, N. K. (1997). *Simplified analytical solution for free drops during NCT for radioactive materials packaging*. US DOE report DE-AC09-96SR18500.

Hallquist, J. O. (2006). *LS-DYNA theory manual*. Livermore Software and Technology Corporation (version 970).

Halstead, R. J., & Dilger, F. (2006). Full-scale cask testing revisited, again. In *WM 2006 conference,* February 27–March 2, Tuscon, AZ, USA.

Hanifehzadeh, M., Gencturk, B., Attar, A., & Willam, K. (2017). Multi-hazard performance of reinforced concrete dry casks subjected to chloride attack and tip-over impact. *Annals of Nuclear Energy, 108,* 10–23.

Hansson, H., & Skoglund, P. (2002). *Simulation of concrete penetration in 2D and 3D with the RHT material model*. Swedish Defense Research Agency.

Hibbitt, Karlsson and Sorensen, Incorporated (2002). *ABAQUS/CAE user's manual*.

Huang, M., & Pietruszczak, S. (1996). Numerical analysis of concrete structures subjected to alkali-aggregate reaction. *Mechanics of Cohesive-Frictional Materials, 1*(4), 305–319.

Huang, C.-C., & Wu, T.-Y. (2009). A study on dynamic impact of vertical concrete cask tip-over using explicit finite element analysis procedures. *Annals of Nuclear Energy, 36*(2), 213–221.

Islam, J., Liu, Z., & Swaddiwudhipong, S. (2011). Numerical study on concrete penetration/perforation under high velocity impact by ogive-nose steel projectile. *Computers and Concrete, 8*(1), 111–123.

Kim, D.-H., Seo, K.-S., Lee, J.-C., Bang, K.-S., Cho, C.-H., Lee, S. J., et al. (2007). Finite element analyses and verifying tests for a shock-absorbing effect of a pad in a spent fuel storage cask. *Annals of Nuclear Energy, 34*(11), 871–882.

Larive, C. (1998). Apportscombin'es de l'experimentation et de la modelisation a la comprehension del' a lcalireaction et de seseffetsmecaniques. PhD Thesis, Thése de Doctorat, Laboratoire Central des PontsetChaussées, Paris.

Lee, Y. S., Ryu, C. H., Kim, H. S., & Choi, Y. J. (2005). A study on the free drop impact of a cask using commercial FEA codes. *Nuclear Engineering and Design, 235,* 2219–2226.

Léger, P., Côté, P., & Tinawi, R. (1996). Finite element analysis of concrete swelling due to alkali-aggregate reactions in dams. *Computers and Structures, 60*(4), 601–611.

LS-DYNA examples manual (2001). Livermore Software Technology Corporation. http://www.lstc.com/download/ls-dyna_%28win%29#pclic.

Malvar, L., Crawford, J., Wesevich, J., & Simons, D. (1997). A plasticity concrete material model for DYNA3D. *International Journal of Impact Engineering*, *19*(9–10), 847.

Montoya, E., Vecchio, F. J., & Sheikh, S. (2006). A compression field modeling of confined concrete: Constitutive models. *Journal of Materials in Civil Engineering, 18*(4), 510–517.

Morris, C., Dangora, L., & Sherwood, J. (2013). Using LS-DYNA to simulate the forming of woven-fabric reinforced composites. In *The 19th international conference on composite materials*, Montreal, Canada.

Mousavi, R., Champiri, M. D., Joshaghani, M. S., & Sajjadi, S. (2016a). A kinematic measurement for ductile and brittle failure of materials using digital image correlation. *AIMS Materials Science, 3*(4), 1759–1772. https://doi.org/10.3934/matersci.2016.4.1759.

Mousavi, R., Champiri, M. D., & Willam, K. (2016). Efficiency of damage-plasticity models in capturing compaction–extension transition of concrete under different compression loading conditions. In *Proceedings of VII European congress on computational methods in applied sciences and engineering (ECCOMAS congress 2016).*

Multon, S., & Toutlemonde, F. (2006). Effect of applied stresses on alkali-silica reaction-induced expansions. *Cement and Concrete Research, 36,* 912–920.

Murray, Y. D. (2007). *Users manual for LS-DYNA concrete material model 159*. Technical report.

Poyet, S., Sellier, A., Capra, B., Foray, G., Torrenti, J. M., Cognon, H., et al. (2007). Chemical modelling of alkali silica reaction: Influence of the reactive aggregate size distribution. *Materials and Structures, 40*(2), 229–239.

Raheem, A. M., & Joshaghani, M. S. (2016). Modeling of shear strength–water content relationship of ultra-soft clayey soil. *International Journal of Advanced Research, 4*(4), 537–545.

Raheem, A. M., Vipulanandan, C., & Joshaghani, M. S. (2017). Non-destructive experimental testing and modeling of electrical impedance behavior of untreated and treated ultra-soft clayey soils. *Journal of Rock Mechanics and Geotechnical Engineering, 9*(3), 543–550.

Saouma, V. E., & Perotti, L. (2006). Constitutive model for alkali-aggregate reactions. *ACI Materials Journal, 103,* 194–202.

Shi, Y., Li, Z.-X., & Hao, H. (2010). A new method for progressive collapse analysis of RC frames under blast loading. *Engineering Structures, 32,* 1691–1703.

Simo, J., Kennedy, J., & Govindjee, S. (1988). Non-smooth multisurface plasticity and viscoplasticity. Loading/unloading conditions and numerical algorithms. *International Journal for Numerical Methods in Engineering, 26*(10), 2161–2185.

Tabiei, A. Contact in LS-DYNA. www.LS-DYNA-online.com.

Tang, E. K. C., & Hao, H. (2010). Numerical simulation of a cable-stayed bridge response to blast loads, Part I: Model development and response calculations. *Engineering Structures, 32,* 3180–3192.

Teng, T. L., Chu, Y. A., Chang, F. A., Chin, H. S., & Lee, M. C. (2003). The dynamic analysis of nuclear waste cask under impact loading. *Annals of Nuclear Energy, 30,* 1473–1485.

Tu, Z., & Lu, Y. (2010). Modifications of RHT material model for improved numerical simulation of dynamic response of concrete. *International Journal of Impact Engineering, 37*(10), 1072–1082.

Ulm, F. J., Coussy, O., Kefei, L., & Larive, C. (2000). Thermo–chemo-mechanics of ASR expansion in concrete structures. *Journal of Engineering Mechanics, 126*(3), 233–242.

Wang, Z., Konietzky, H., & Huang, R. (2009). Elastic–plastic-hydrodynamic analysis of crater blasting in steel fiber reinforced concrete. *Theoretical and Applied Fracture Mechanics, 52*(2), 111–116.

Wang, Z., Wu, J., & Wang, J. (2010). Experimental and numerical analysis on effect of fibre aspect ratio on mechanical properties of SRFC. *Construction and Building Materials, 24*(4), 559–565.

Wu, K.-C., Li, B., & Tsai, K.-C. (2011). The effects of explosive mass ratio on residual compressive capacity of contact blast damaged composite columns. *Journal of Constructional Steel Research, 67,* 602–612.

Xu, K., & Lu, Y. (2006). Numerical simulation study of spallation in reinforced concrete plates subjected to blast loading. *Computers and Structures, 84*(5), 431–438.